JGR Solid Earth

RESEARCH ARTICLE
10.1029/2024JB030914

Microstructural Evolution of Carrara Marble During Semi-Brittle Deformation

Tongzhang Qu[1], **Nicolas Brantut**[1,2], **David Wallis**[3], **and Christopher Harbord**[1,4]

[1]Department of Earth Sciences, University College London, London, UK, [2]GFZ German Center for Geosciences, Potsdam, Germany, [3]Department of Earth Sciences, University of Cambridge, Cambridge, UK, [4]Severn Trent Plc, Coventry, UK

Key Points:

- With axial strain up to 2%, hardening is high, twins accommodate most axial deformation, and fracture intensity increases rapidly in marble
- Beyond 2% strain, hardening decreases, twins and cracks accumulate less rapidly, and geometrically necessary dislocation density increases
- Yield stress and overall strength depend strongly on temperature between 20°C and 200°C, indicating that dislocation glide controls strength

Supporting Information:

Supporting Information may be found in the online version of this article.

Correspondence to:

T. Qu,
tongzhang.qu@ucl.ac.uk

Citation:

Qu, T., Brantut, N., Wallis, D., & Harbord, C. (2025). Microstructural evolution of Carrara marble during semi-brittle deformation. *Journal of Geophysical Research: Solid Earth*, *130*, e2024JB030914. https://doi.org/10.1029/2024JB030914

Received 10 DEC 2024
Accepted 22 JUL 2025

Author Contributions:

Conceptualization: Tongzhang Qu, Nicolas Brantut, Christopher Harbord
Data curation: Tongzhang Qu, Nicolas Brantut
Formal analysis: Tongzhang Qu
Funding acquisition: Nicolas Brantut, David Wallis
Investigation: Tongzhang Qu, Nicolas Brantut, David Wallis
Methodology: Tongzhang Qu, Nicolas Brantut, David Wallis, Christopher Harbord
Project administration: Nicolas Brantut, David Wallis
Resources: Nicolas Brantut, David Wallis
Software: David Wallis
Supervision: Nicolas Brantut

Abstract Fifteen marble samples were subjected to semi-brittle deformation through triaxial compression experiments, reaching axial strains of about 0.5%, 1.0%, 2.0%, 4.0%, or 7.5% at temperatures of 20°C, 200°C, or 350°C, under a confining pressure of 400 MPa. Deformation twins, lattice curvature, and intragranular microfractures in the samples were quantitatively characterized using forescattered electron images and electron backscatter diffraction. Microstructural analyses revealed that twins accommodate most of the shortening during the first 2% strain, whereas lattice curvature associated with geometrically necessary dislocations predominantly develops with more strain. Intragranular fracture intensity exhibits an almost linear correlation with strain during the first 2% strain but increases more gradually with strain thereafter. The mechanical data indicate a strong decrease of yield stress with temperature increasing between 20°C and 200°C, consistent with the temperature dependence of the critical resolved shear stress for dislocation glide. The post-yield strain hardening is likely caused by progressively increasing intensity of interactions among dislocations and between dislocations and twin boundaries. Based on the microstructural data and interpreted hardening mechanisms, we propose a phenomenological model, with state variables representing microstructural elements that hinder dislocation glide, as a step toward development of a microphysical constitutive model of semi-brittle deformation.

Plain Language Summary In the shallow crust, rocks tend to crack or break when stressed. With increasing depth, elevated pressure and temperature cause rocks to bend or flow instead. However, it is not clear what controls the strength of the crust during the transition. In particular, the roles of several deformation processes and how they interact are unknown. We deformed rocks at an elevated pressure and a range of temperatures in laboratory, and quantify how different processes developed at different deformation stages. To achieve this, we squeesed samples of calcite marble to different extents of deformation, and we imaged tiny cracks and internal crystal changes after deformation using electron-microscopy techniques. Our work shows that different mechanisms are activated in sequence, with a lot of cracking and crystal reorgnisation (twinning) at low strain. At large strain, there is a substantial increase in crystal bending (dislocation activity). We find that the overall strength is most likely controlled by motion of crystal defects (dislocations), which is the hardest deformation mechanism in the conditions tested. We suggest that our data set can be used to develop a model for mechanical behavior of calcite rocks, as a precursory basis for modeling deformation in the Earth's mid crust.

1. Introduction

As pressure and temperature increase with depth, the mechanical behavior of the lithosphere undergoes a transition from primarily pressure-dependent frictional processes and associated brittle behavior to primarily temperature-dependent crystal-plastic deformation (Brace & Kohlstedt, 1980; Kohlstedt et al., 1995). At depths spanning this transition of mechanical behavior, the concurrent operation of brittle and crystal-plastic processes, referred to as semi-brittle deformation, is evidenced by a broad range of field observations from outcrops of exhumed mid-crustal rocks (e.g., Bak et al., 1975; Fagereng & Sibson, 2010; Passchier, 1982; Sibson, 1977; White & White, 1983). Understanding of semi-brittle deformation is of fundamental importance to modeling deformation of the lithosphere as the semi-brittle regime is where the strength of rocks is greatest. Thus, semi-brittle deformation exerts a key control on several aspects of geodynamics, including integrated plate strength (Kohlstedt et al., 1995), the depth extent of the seismogenic zone (Carpenter et al., 2016; Shimamoto, 1986; Sibson, 1982), and characteristics of lithospheric flexure (Chapple & Forsyth, 1979; Sandiford & Craig, 2023).

Validation: Tongzhang Qu
Visualization: Tongzhang Qu
Writing – original draft: Tongzhang Qu
Writing – review & editing: Tongzhang Qu, Nicolas Brantut, David Wallis, Christopher Harbord

Quantitative characterization of the complex interplay of deformation mechanisms operating during semi-brittle deformation requires combined efforts from laboratory experimentation, microstructural observation, and micromechanical modeling. Calcite aggregates have been frequently chosen as the experimental material to study semi-brittle deformation (e.g., Fredrich et al., 1989; Harbord et al., 2023; Olsson, 1974; Rybacki et al., 2021), not only because calcite is an important rock-forming mineral, but also because the pressures and temperatures required for semi-brittle deformation of calcite aggregates are more accessible in experiments than those required for semi-brittle deformation of silicates. Experimentation with monomineralic calcite aggregates also avoids the complexity of semi-brittle deformation in polymineralic aggregates (Pec et al., 2016). At the macroscopic scale, semi-brittle deformation of calcite aggregates is characterized by strain-hardening flow with an absence of localized failure (e.g., Fredrich et al., 1989). Qualitative microstructural characterization of marble samples tested in the semi-brittle regime has revealed concurrent operation of twinning, dislocation activity, and microfracturing (Carter & Kirby, 1978; Fredrich et al., 1989; Olsson & Peng, 1976; Rybacki et al., 2021, and references therein). Correspondingly, quantitative measurements have been made of three main microstructural parameters, specifically twin density (e.g., Rutter, 1983; Rutter et al., 2022; Rybacki et al., 2013), dislocation density (e.g., de Bresser, 1996; Fredrich et al., 1989), and fracture density/intensity (e.g., Fredrich et al., 1989; Harbord et al., 2023).

Despite the previous efforts, a robust constitutive model for semi-brittle deformation remains elusive for two main reasons. First, the evolution of microstructures with macroscopic strain has not been well captured. This limitation is because most previous work focused on the microstructures of marble at similar strains but different pressure-temperature conditions (Fredrich et al., 1989; Harbord et al., 2023; Rybacki et al., 2021), lacking a systematic investigation of microstructures at different strains under the same experimental conditions. Due to the interplay between microfractures and other crystal defects, the evolution of microstructures with macroscopic strain cannot be predicted quantitatively based on existing knowledge of purely frictional or crystal-plastic deformation. Second, there is no consensus on the relationships among mechanical properties and microstructures during semi-brittle deformation. Numerous hardening mechanisms can be activated, including increasing the number of obstacles to dislocation glide (Rybacki et al., 2021), increasing resistance to frictional sliding of microfractures under confinement (Walsh, 1965), and increasing intergranular back stress at twin tips (Burkhard, 1993). The relative importance of each mechanism is currently unclear. As such, quantitative rheological models for semi-brittle flow are either entirely phenomenological (Covey-Crump, 1994) or dependent on strongly simplifying assumptions and poorly constrained microstructural quantities (Horii & Nemat-Nasser, 1986; Liu & Brantut, 2023; Nicolas et al., 2017).

Given these limitations of previous studies, we aim to provide quantitative constraints on the development of brittle and crystal-plastic microstructures in marble undergoing semi-brittle deformation. We conducted triaxial compression experiments on samples of Carrara marble to different axial strains up to 7.5%, covering stages of yielding to post-yield strain hardening, at temperatures of 20°C, 200°C or 350°C and a confining pressure of 400 MPa. The post-mortem samples deformed to different strains were characterized by forescattered electron (FSE) images and electron backscatter diffraction (EBSD). Comprehensive microstructural information, including twin density, twin spacing, geometrically necessary dislocation density, and fracture intensity, was collected as a function of macroscopic strain and temperature. We relate the mechanical data to the microstructural data by interpreting the micromechanical mechanisms for the onset of inelasticity and subsequent strain hardening. Based on our interpretations, we propose a phenomenological model with the collected microstructural quantities as state variables to serve as a guide to the development of future microphysical constitutive models.

2. Methods

2.1. Experimental Materials

The experimental material for this study was Carrara marble. This marble is almost exclusively composed of polycrystalline calcite (>99%), with <1% porosity and no crystallographic preferred orientation. Most grains in Carrara marble are free of twins and other deformation microstructures. A small proportion of grains contain pre-existing thick twins, ≥5 μm in width, which are distinguishable from the thin deformation twins, ≤2 μm in width, that are typically imparted during deformation experiments (e.g., Burkhard, 1993). Mechanical testing has demonstrated good reproducibility across samples deformed under similar experimental conditions (e.g., Rybacki

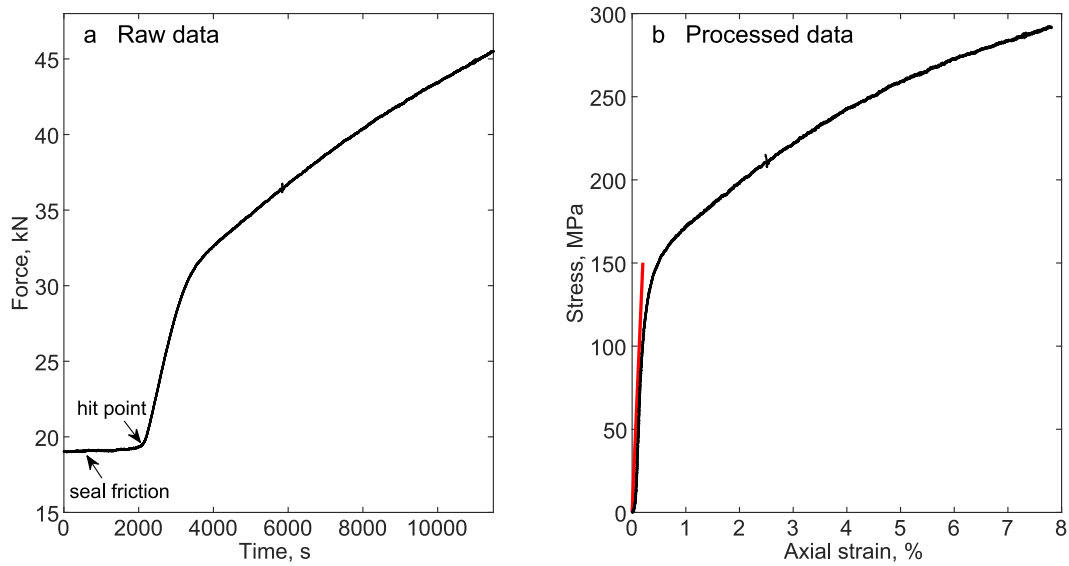

Figure 1. (a) Raw data from Run 244 at a temperature of 350°C and confining pressure of 400 MPa. (b) Processed stress-strain data from Run 244 in black. The red line is estimated stress from the Voigt-Reuss-Hill average Young's modulus (E_0) at the same pressure and temperature for reference. The raw data and stress-strain data in this study are plotted as dots. The apparent thicknesses of the curves reflect the scatter of mechanical data.

et al., 2021). The cylindrical samples of 9.8 mm in diameter used in this study were drilled from a single block of Carrara marble and ground to a length of 22 mm. After cleaning with water, the samples were dried in an oven at 70°C for at least 30 hr before mechanical testing.

2.2. Mechanical Testing

We conduced triaxial deformation experiments in the recently refurbished Murrell gas-medium apparatus at University College London (Edmond & Murrell, 1973; Harbord et al., 2022; Murrell et al., 1989). Details of the refurbishment are provided by Harbord et al. (2022). Before deformation experiments, each cylindrical sample was sandwiched between two disk-shaped Inconel spacers, each 10 mm in diameter and 5 mm in height. The sample and Inconel disks were loaded into an annealed copper jacket that was 0.2 mm thick and 50 mm in length with an inner diameter of 10.5 mm. Two Inconel pistons were inserted into the two ends of the copper jacket loaded with the sample and disks. Two Inconel rings were swaged over the contact between the copper jacket and the Inconel pistons. To limit overstretching and avoid puncture of the jacket, a small amount of molybdenum disulfide was applied to the outer surface of the copper jacket before swaging. The resulting collapse of the copper jacket onto the Inconel pistons provided a gas seal for the sample during mechanical testing. The high yield stress of Inconel at high temperatures, greater than 700 MPa at temperatures below 500°C (Guthrie et al., 1990), ensures transmission of load in the following mechanical testing.

The specimen assembly was screwed on a steel piston and loaded through a series of Bridgeman seals into the deformation apparatus (Edmond & Murrell, 1973; Murrell et al., 1989). Confining pressure was achieved by pumping Ar into the pressure vessel with Bridgeman seals between the vessel liner and the steel piston. The top of the steel piston was located outside of the pressure vessel. Elevated temperatures at the sample were achieved by a furnace within the pressure vessel and calibrated at the target temperatures before mechanical experiments (details of furnace calibration are in the Supporting Information S1). The differential axial force was applied by a servo hydraulic actuator located vertically above the pressure vessel and transmitted through an external load cell onto the top of the steel piston. The precision of force measurement is on the order of 0.1 kN, indicated by the scatter of raw data in Figure 1a. The shortening of the specimen assembly was measured by a pair of RDP GT5000-L25 linear variable differential transducers, with a precision of 150 nm, attached to the top steel piston (Figure 2 of Harbord et al., 2022).

The raw data of axial force and displacement, both measured externally from the pressure vessel, required corrections to obtain stress and strain of the sample (Figure 1). First, the seal friction and strength of the copper

Table 1
Summary of Mechanical Testing

Run	Temperature, °C	ε[a], %	σ[a], MPa	Hardening modulus[b], GPa
241	20	0.6	260	15.1
239	20	1.0	307	8.5
238	20	2.1	335	2.4
237	20	4.1	366	1.9
242	20	7.8	437	1.2
222	200	0.3	136	26.7
221	200	1.1	167	4.3
225	200	1.8	213	3.2
223	200	3.8	264	2.9
89	200	7.5	300	0.8
249	350	0.5	146	10.4
247	350	0.8	149	4.7
246	350	2.0	189	2.7
248	350	4.0	226	1.3
244	350	7.8	292	0.6

[a]ε and σ are strain and stress data at the end of loading, respectively. [b]Hardening modulus here was calculated from the final 0.1%–0.2% strain before unloading by Equation 1.

jacket were subtracted from the raw force data. The seal friction was found to be dependent on pressure and displacement rate. Here, a constant confining pressure of 400 MPa and displacement rate of 220 nm/s, corresponding to a strain rate of 1×10^{-5} s^{-1} for the original length of the sample, were applied during all the experiments in this study. Seal friction along the loading piston was estimated using the axial force before the hit point (Figure 1a). The strength of the jacket was calculated as the flow law of Frost and Ashby (1982) (details in the Supporting Information S1). The stress on the sample was calculated by the corrected force divided by the cross-sectional area of the sample, which was assumed to increase linearly with deformation with no volumetric expansion. The externally measured displacement data were corrected for elastic distortion of the Inconel piston assembly.

Sets of experiments were conducted at three different temperatures; one each at room temperature, 200°C and 350°C. In each set of experiments, loading was ceased at axial strains of about 0.5%, 1.0%, 2.0%, 4.0% or 7.5%. In total, 15 samples were tested (Table 1). We included Run 89% to 7.5% strain at 200°C, which is a previous experiment with the same apparatus at the same strain rate and pressure by Harbord et al. (2023).

The hardening modulus (H) was computed from the slope (k) of the stress-strain curve and the Young's modulus of intact calcite aggregates (E_0) by

$$H = \left(k^{-1} - E_0^{-1}\right)^{-1}. \quad (1)$$

The slope of the stress-strain curve was calculated by linear regression over the last 100–200 stress-strain data for each experiment, covering a range of 0.1%–0.2% axial strain at about 0.5%, 1.0%, 2.0%, 4.0% and 7.5% axial strain before unloading. We found relatively large variability of the slopes at the start of loading in stress-strain curves. Such variation in initial slopes arises from manually selecting hit points within segments exhibiting a gradual slope transition in the force-displacement curves (Figure 1a). Furthermore, this hit point selection method can introduce stress measurement uncertainty of up to 10 MPa, depending on the curvature of the force-displacement curve near the hit point. Thus, instead of extracting Young's modulus from experimental measurements, the Young's modulus E_0 was approximated by the Voigt-Reuss-Hill average of moduli for single crystals of calcite across all orientations. The Voigt and Reuss bounds for calcite's trigonal symmetry were calculated following Watt and Peselnick (1980). The elastic moduli of calcite at a confining pressure of 400 MPa and temperatures from 20°C to 350°C were extracted from Dandekar (1968) and Lin (2013). Details of the calculation are in the Supporting Information S1.

The accuracy of H is limited by the measurement of axial load external to the pressure vessel and seals. During the loading process, the steel piston, transmitting force from the actuator to the specimen assembly, horizontally expands due to the Poisson effect, which could lead to an increase in friction at the piston seal. The magnitude of this increase is expected to be minor relative to our correction for seal friction, but might not be negligible in the calculation of hardening modulus. Accordingly, the reported hardening moduli are upper bounds on the true hardening moduli.

2.3. Microstructural Characterization

After deformation experiments, the samples were cut into halves from the center of their top surface along the long axis of each sample. The halved samples were impregnated with epoxy in a vacuum chamber to minimize the possibility of introducing fractures during subsequent polishing. Each epoxy block with an exposed axial plane was ground with #1,000 sandpaper then polished with a Buehler™ MiniMet® 1000 with progressively finer diamond pastes from 15 μm down to 0.25 μm. Colloidal silica was used for final polishing. After polishing, the samples were coated with approximately 5 nm of carbon.

Microstructural data were acquired on a Zeiss Gemini™ 300 field emission gun scanning electron microscope in the Department of Materials Science and Metallurgy, University of Cambridge. The polished surface was tilted to

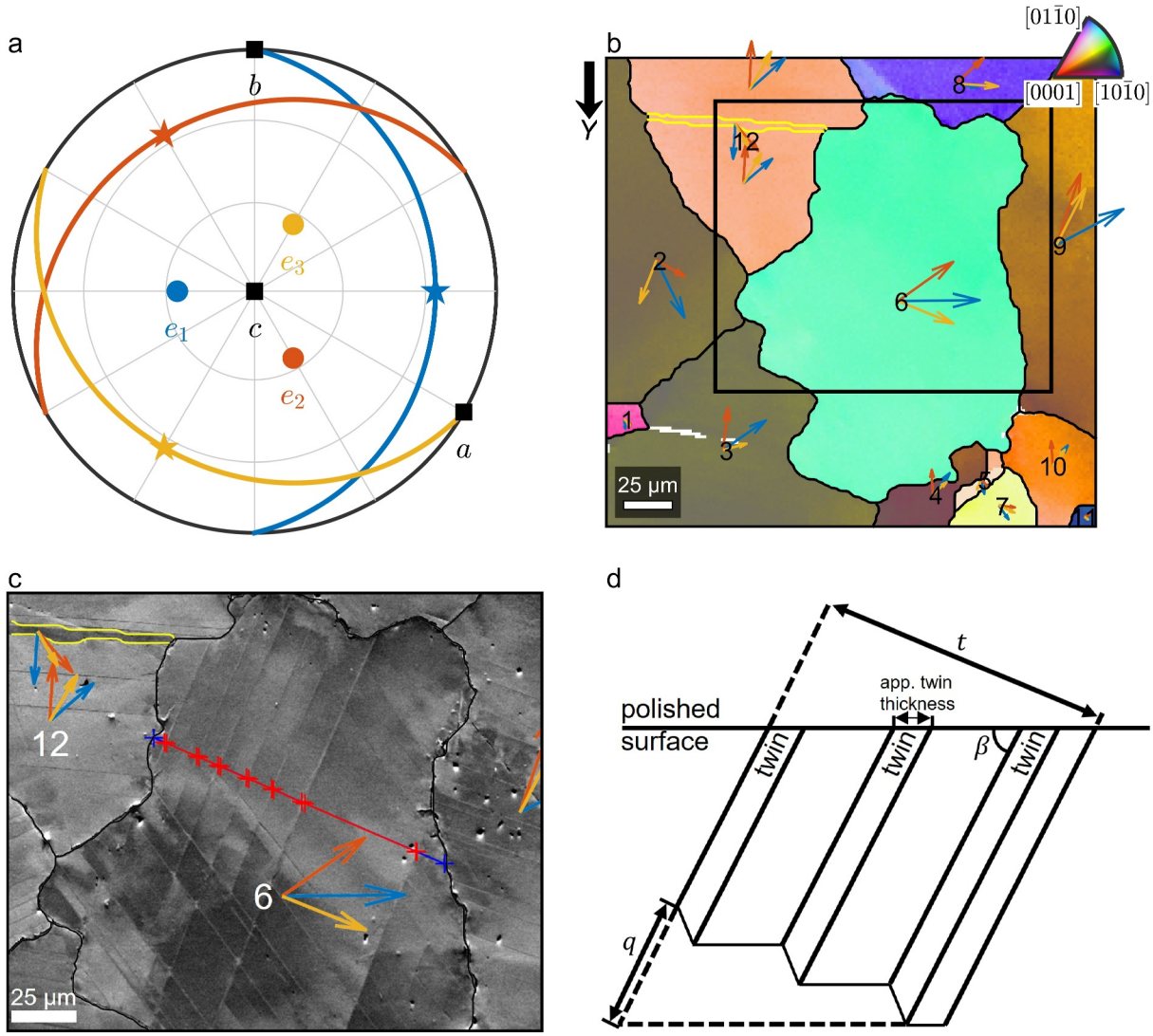

Figure 2. (a) Crystallography of *e* twins in calcite. Axes *a*, *b* and *c* define a fundamental region for calcite. *e* planes and poles for three twin sets (e_1, e_2, e_3) are colored as solid lines and circles, respectively. The twin shear directions *g* are indicated by stars. For each twin, the *e* pole, *c* axis, and corresponding shear direction are co-planar. (b) Selected subarea of the EBSD map of the sample from Run 225. Yellow lines mark the twin boundaries identified by EBSD. Black lines mark grain boundaries. The color of each pixel is based on the crystal direction parallel to the *Y* axis (direction indicated by the black arrow) according to the color key in the top-right corner. This color scheme is also applied to other orientation maps in this study. Each grain is identified by a number. The three arrows in each grain (or twinned portion) are projections of the three *e* poles from 3D into the plane of the map. The color of each arrow corresponds to the color of *e* poles in panel (a). (c) FSE image of part of the mapped area marked by the black rectangle in panel (b). The apparent twin thicknesses and twin spacings are determined from the coordinates of the red crosses. The distance between the blue crosses records the grain width. The twin boundaries of the measured twin set in Grain 6 are perpendicular to the yellow arrow corresponding to e_3, whereas the other twin set in this grain is perpendicular to the orange arrow for e_2. (d) Schematic illustration of twinned calcite in cross section. *q* is the shearing distance from twinning, *t* is the thickness of the grain, and β is the inclination angle between the polished surface and a twin-boundary *e* plane.

70° within the vacuum chamber. Forescattered electron (FSE) images were acquired at an accelerating voltage of 30 kV, with an aperture 120 μm in diameter, at a working distance of 15 mm. The vertical and horizontal position of a scintillator detector with FSE diodes remained the same for all FSE images. EBSD mapping was conducted under the same conditions with a step size of 1.5 μm using an Oxford Instruments Symmetry EBSD detector and AZtec™ 4 acquisition software. For each sample, an FSE image with a width of 1.5 mm and height of 1.0 mm was collected near the center of the polished surface, then an EBSD map of the same size was collected at the same location.

Maps from EBSD were processed with the MATLAB toolbox MTEX v5.8.1. The crystal symmetry was defined as −3 m1 with $a = 5$ Å, $b = 5$ Å and $c = 17$ Å. The reference frame was chosen to be $x \parallel a^*$, $y \parallel b$, $z \parallel c^*$ (Figure 2a). Here axes *x*, *y*, *z* form an orthogonal crystal coordinate system as the reference frame. a^* and c^* refer

to the reciprocal crystal coordinate system. In the coordinate frame of the physical specimen, we denote Y the axis pointing downwards in the direction of the macroscopic axial stress, and Z the axis pointing into the plane of the EBSD maps. Any indexed pixels with fewer than 2 adjacent indexed pixels were removed as noise. Any pixels that were not indexed but had at least one indexed neighbor were filled with the average orientation of the neighboring indexed pixels. After data cleaning, calcite grains were reconstructed from EBSD maps with a threshold misorientation angle of 10° between neighboring indexed pixels defining grain boundaries. M index is calculated as the measure of crystallographic preferred orientation of all the grains in each EBSD map (Skemer et al., 2005). The procedures to acquire key microstructural information, on mechanical twins, lattice curvature, and intragranular microfractures, are described below.

2.3.1. Mechanical Twins

In the crystal coordinates of the hexagonal structural cell for calcite, e twins are formed on $\{10\bar{1}8\}$ e planes and shear in $\langle 40\bar{4}1\rangle$ directions (Figure 2a). We collected data on twin density (i.e., number of twins per unit length), twin spacing, twin thickness, and strain accommodated by twins.

In EBSD maps, the twin boundaries are defined by boundaries between neighboring portions of crystal with misorientation angles of $77.9 \pm 4°$, that is, close to the misorientation angle between a parent grain and e twin in calcite, around crystal axes $\langle\bar{1}104\rangle$. The tolerance of 4° allows for imprecision in the measurements (on the order of 0.1°, the angular resolution for misorientation angles in EBSD) plus any possible intragranular misorientation that may be present between measurement points due to dislocations and fractures. As the widths of most deformation e twins are thinner than 2 μm, the pixels within them are commonly separate and therefore removed by noise reduction, whereas the thicker pre-existing e twins are better resolved (see an example in Figures 2b and 2c). Accordingly, the information on thin mechanical twins is best obtained by manual measurements on FSE images (Figure 2c; Rutter et al. (2022)). First, a twin boundary is manually traced. Second, a straight line perpendicular to the trace, crossing all the twin boundaries of this set, is drawn. Third, the coordinates of the intersections between twin boundaries and the crossing line are manually picked to calculate the apparent twin thickness and the apparent spacings between two adjacent twins (i.e., twin spacing).

The true twin spacings and twin thicknesses can also be calculated from the locations of twin boundaries. A schematic cross section of twins is plotted in Figure 2d. The apparent twin thicknesses and spacings were acquired as described above. However, twin boundaries, as planes, intersect with the polished surface of the sample by an inclination angle β. Quantification of the true twin spacing and thickness, that is the distances perpendicular to twin boundaries, requires the value of β for each twin set. We obtain β by extracting combined information from FSE images and EBSD maps following Rutter et al. (2022). The average orientation of the c axis in X-Y-Z specimen coordinates is obtained from the mean orientation of all pixels in the grain. Thus, the three possible e poles can be computed based on the crystallography in Figure 2a projected onto the 2D map as in Figure 2b and overlapped with the FSE image in Figure 2c. The orthogonal relation between the projection of one of the three e poles and the twin boundaries of interest in Figure 2c determines the orientation of the e pole of the observed twin system. The inclination angle β for the twin set of interest is equivalent to the angle between this e pole (normal to the twin boundaries) and the Z axis (normal to the polished surface). The true twin spacing and thickness can then be calculated from the apparent spacing and inclination angle β.

Twinning causes simple shear (Figure 2d). The engineering shear strain (γ) that results from twinning is calculated as the ratio between shearing distance (q) and the true width of the grain (t). Following the crystallographic relation between e-twin normals and the c axis in Figure 2a, the angular relation between the twins and the host grain is constant. As such, q can be calculated from the sum of twin thicknesses and this constant angle, and therefore the engineering shear strain γ resulting from twinning in each grain is given by

$$\gamma = \frac{q}{t} = \frac{2}{t}\sum_{k=1}^{n} t_k \tan\left(\frac{\alpha}{2}\right), \tag{2}$$

where q is calculated from the sum of twin thickness ($\sum_{k=1}^{n} t_k$, where k indexes each individual twin, n is the total number of one set of e twins in each grain) and the constant angular change ($\alpha = 37.28°$) of a $\{10\bar{1}4\}$ plane as a consequence of twinning (Groshong, 1972).

The optimal directions of shortening (C) and lengthening (T) were determined based on the crystal symmetry of calcite. The C axis is oriented at 45° to the twin-shear direction, and the T axis is oriented at 45° to the e pole, both in a clockwise manner within the plane containing the e plane normal and g in Figure 2a. The strain tensor in C-T coordinates is

$$\boldsymbol{\varepsilon}_{\mathrm{CT}} = \begin{bmatrix} \gamma/2 & 0 & 0 \\ 0 & -\gamma/2 & 0 \\ 0 & 0 & 0 \end{bmatrix}, \tag{3}$$

with positive component parallel to T axis and negative component parallel to C axis. $\boldsymbol{\varepsilon}_{\mathrm{CT}}$ can be converted to a strain tensor in X-Y-Z specimen coordinates ($\boldsymbol{\varepsilon}_{\mathrm{t}}$) by

$$\boldsymbol{\varepsilon}_{\mathrm{t}} = \gamma \mathbf{G}, \tag{4}$$

where the matrix $\mathbf{G}$ contains the cosines between C-T axes and X-Y-Z axes (Groshong, 1972), transferring the engineering shear strain γ in crystal coordinates into the strain tensor ε_{t} in specimen coordinates.

Overall, we collected microstructural information on twin lamellae from 28 to 46 grains from the FSE images and EBSD maps of each sample, including twin density, true twin spacing, true twin thickness and strain accommodated by twins $\boldsymbol{\varepsilon}_{\mathrm{t}}$. The twin density of each sample is calculated as the total number of measured twins over the total length of measured grain widths. The average true twin spacing and thickness are considered as representative values for each sample. The YY element in the strain tensor $\boldsymbol{\varepsilon}_{\mathrm{t}}$, denoted as $\varepsilon_{\mathrm{tYY}}$, indicates the shortening (positive value) or lengthening (negative value) accommodated by e twins in the direction of macroscopic applied stress of individual grains. The average value of $\varepsilon_{\mathrm{tYY}}$ for each sample is calculated as the weighted average of the $\varepsilon_{\mathrm{tYY}}$ from the measured grains, using grain areas as weighting factors.

For grains with more than one twin set, all the twin information was collected for each twin set. The highest twin density among the measured twin sets in each grain was considered the representative value. The true twin spacing and twin thickness are the averages of all the measurements. $\varepsilon_{\mathrm{tYY}}$ is the sum of all the $\varepsilon_{\mathrm{tYY}}$ from different twin sets in these grains.

The number of these measured grains is only a small portion of the total number in a bulk sample, and the extent of twinning varies among the grains. Accordingly, to evaluate how representative these measurements are of the characteristics of the bulk sample, we use a bootstrap method to calculate the standard deviation of distributions from resampling of these measurements. The measured grains of each sample are randomly sampled with replacement into a test set with size the same as the number of selected grains from each map. The twin information of this test set is calculated as described above. This procedure of randomly choosing grains and calculating twin information is run iteratively 10,000 times for each sample. This resampling strategy provides a normal distribution of each type of twin information. The standard deviation of this distribution is considered as the uncertainty of these measurements for the bulk sample.

2.3.2. Lattice Curvature

Our approach to evaluate lattice curvature associated with dislocations is introduced in this subsection. EBSD measurements provide the crystal orientation at each point in specimen coordinates. The misorientation angle $\mathrm{d}\theta$ between any two points is defined as a rotation angle about a common axis determined as a unit vector (uvw) in crystal coordinates (cf., Figure 4 in Muransky et al., 2019). Lattice curvature κ_{ij} is defined as the infinitesimal misorientation $\mathrm{d}\theta_i$ across an infinitesimal displacement $\mathrm{d}u_j$ along an axis in specimen coordinates ($i = 1, 2, 3$ for x, y, z axes, respectively; $j = 1, 2, 3$ for X, Y, Z axes, respectively) as

$$\kappa_{ij} = \frac{\mathrm{d}\theta_i}{\mathrm{d}u_j}, \tag{5}$$

where

$$d\theta_1 = |d\theta|\frac{u}{\sqrt{u^2+v^2+w^2}}, d\theta_2 = |d\theta|\frac{v}{\sqrt{u^2+v^2+w^2}}, d\theta_3 = |d\theta|\frac{w}{\sqrt{u^2+v^2+w^2}}. \quad (6)$$

With the assumption that spatial gradients in elastic strain are negligible, the lattice curvature κ_{ij} results from the presence of dislocations (Nye, 1953). Accordingly, in theory, it is possible to acquire the density of each type of dislocation from lattice curvature.

In practice, EBSD maps can only offer limited information on lattice curvature and thus dislocations. Firstly, EBSD maps are collected with a finite step size (here, 1.5 μm). As such, dislocations with opposite signs of Burgers vector between two neighboring pixels (i.e., statistically stored dislocations, SSD) do not contribute to the lattice curvature from EBSD maps. Instead, only the portion of dislocations with a nonzero sum of Burgers vectors can be captured, termed geometrically necessary dislocations (GND). Secondly, curvature in the direction of the Z axis ($j = 3$; normal to the map) cannot be accessed with a 2D map, and thus only six elements of κ_{ij} in the 2D plane containing the X and Y axes can be directly measured by EBSD. Thirdly, calcite has more than six slip systems (de Bresser, 1991), thus the solution of dislocation densities for individual dislocation types from the incomplete lattice curvature is non-unique. Lastly and most importantly, the angular resolution of the conventional EBSD data (on the order of 0.1°) can obscure GND densities in pixel-level calculations, in which the length scale over which curvature is measured is typically relatively short. Accordingly, instead of resolving dislocation density from pixel-to-pixel measurements, we used a simplified approximate relation between misorientation at the grain scale and GND density from Ashby (1970) to estimate ρ_{GND},

$$\rho_{GND} = \frac{\theta_m}{bd}, \quad (7)$$

where θ_m is the misorientation angle at the grain scale, b is the average length of the available Burgers vectors, and d is grain size. We used the grain orientation spread (GOS) as an estimate of θ_m, calculated by

$$\theta_m = \mathrm{GOS} = \frac{1}{m}\sum_{l=1}^{m}\theta_l, \quad (8)$$

where m is the number of pixels in a grain, and θ_l is the misorientation angle between the orientation of the lth pixel and the mean orientation of the grain. To be consistent with using GOS as the measure of misorientation at the grain scale, d in Equation 7 is also replaced by the average of the distance between each pixel and the grain centroid, d_c. Overall, we have

$$\rho_{GND} = \frac{\mathrm{GOS}}{bd_c} \quad (9)$$

as an estimate of the minimum density of GND for each grain. As such, by increasing the length scale over which curvature is measured up to the scale of the grain size, we can improve the signal-to-noise ratio for estimates of lattice curvature and GND density. To acquire ρ_{GND} for the entire EBSD map as the representative ρ_{GND} for the sample, ρ_{GND} of each grain is multiplied by the individual grain area, the sum of which is normalized by the whole map area. Each map contains 200–300 grains, and no manual operation or non-uniqueness is involved in data acquisition.

2.3.3. Intragranular Microfractures

Fractures visible in FSE images were traced in ImageJ by recording the coordinates of the ends of a fracture and the nodes where the fracture direction changes. The tracing results were analyzed with the MATLAB® toolbox FracPaQ v2.8 (Healy et al., 2017). As most grain boundaries are open in Carrara marble after decompression and polishing (Harbord et al., 2023), only intragranular fractures of the experimentally deformed samples were traced. Fracture intensity is calculated as the sum of fracture lengths over the image area.

The result of tracing fractures is highly dependent on the image quality, which is influenced by many factors, including the thickness of the carbon coat and the focus of the electron beam. In addition, this traced map

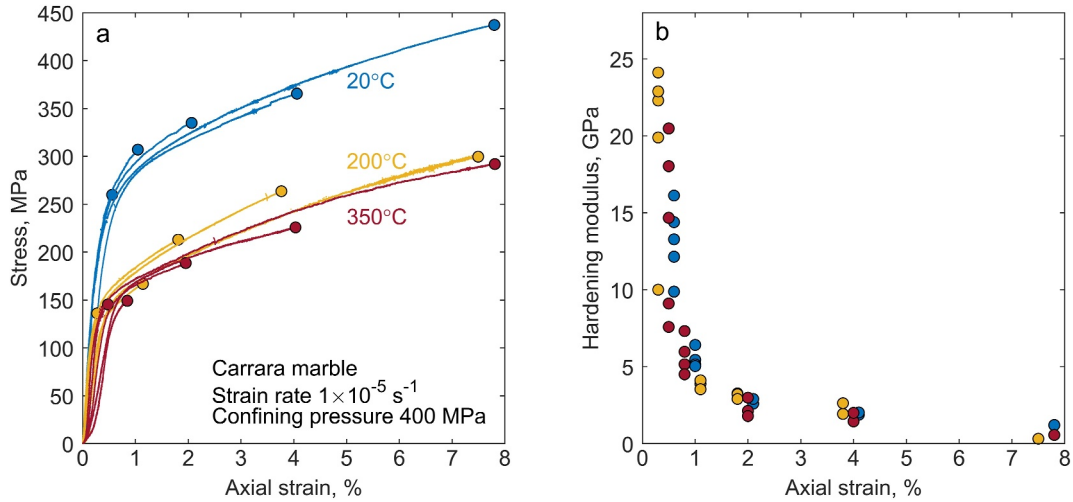

Figure 3. (a) Stress-strain data at three experimental temperatures. Temperatures are color coded. The end of loading in each experiment is highlighted by a circle, summarized as ε and σ in Table 1. (b) Hardening modulus against strain derived by Equation 1 from each stress-strain curve in panel (a) and the Young's modulus from the Voigt-Reuss-Hill average stiffness of calcite at the experimental conditions. The colors in panel (b) follow the color code in panel (a). Hardening modulus against stress providing similar information is added as Figure S4 in Supporting Information S1.

represents only a portion of the sample. To evaluate whether the fracture intensity determined from the image area is representative of the bulk sample, we divided each FSE image into 100 strips. The width of each strip is the same as the width of the complete image (1.5 mm), and the height of each strip is 1/100 of the image height (i.e., 10 μm). The traced fractures were assigned into each strip based on their node locations. This subdivision revealed that with 25 randomly chosen strips the fracture intensity is close (within about ± 5%) to the fracture intensity of the whole map. For this reason, 100 testing blocks, each with a quarter of the image area, were randomly distributed onto each FSE image. The distribution of fracture intensity from all the testing blocks is used for calculating a standard deviation as the uncertainty of the measurement of fracture intensity for each sample.

Cleavage fractures were identified by an approach similar to that used to identify twin sets. The normal of each of the three cleavage planes (i.e., r planes $\{10\bar{1}4\}$) was projected onto each grain in the 2D EBSD maps. When the section between two nodes of a traced fracture is at an angle of 90 ± 10° to one of the projected cleavage normals (where the range allows for imprecision in tracing), the section of traced fracture is assigned as cleavage.

3. Results

3.1. Mechanical Testing

The mechanical testing results are summarized in this section, including stress-strain curves and hardening modulus (Figure 3) and stress-strain data at the end of loading (Table 1) at 20°C, 200°C and 350°C. Temperature has an overall weakening effect on the samples. With the difference in temperature between 20°C and 200°C, the stress at a given axial strain decreases by about 100–150 MPa. However, the difference in temperature between 200°C and 350°C produces only a modest decrease in strength.

The mechanical behavior of Carrara marble exhibits systematic strain hardening with common features observed at the three temperatures. The stress-strain data at the three temperatures display linear segments at strains <0.2%. At about 0.5%–1% axial strain, the slope of the stress-strain curves decreases markedly, and beyond about 1% axial strain the slope continues to decrease but at a lesser rate. These trends are quantified by the hardening modulus, which exhibits a sharp decline with increasing axial strain up to 1%–2%, followed by a more gradual decrease between 2% and 8% axial strain (Figure 3b). The hardening modulus does not exhibit a resolvable temperature dependence.

3.2. Microstructures

Inelastic strain in the deformed marble samples is recorded as mechanical twins, lattice curvature, and microfractures. As strain increased, these three types of microstructures developed as demonstrated by Figures 4a–4d for marble samples tested at a temperature of 200°C. No/few transgranular fractures are present. There are no spatial relationships indicative of lattice curvature having been induced by cracks, nor vice versa. Lattice curvature was found to be strong at grain contacts at the early stage of deformation, indicated by blue arrows in Figure 4a. As strain develops, lattice curvature is either segmented by twin boundaries (indicated by the blue arrows in Figure 4d) or continues uninterrupted across twin boundaries (indicated by the blue arrows in Figure 4f). The FSE images do not exhibit substantial differences in microstructures among samples deformed at temperatures of 20°C, 200°C or 350°C to the same strain (e.g., a strain of 7.5% in Figures 4d–4f). From the mean orientations of grains in EBSD maps, the M indices of crystallographic preferred orientations, ranging from 0.003 to 0.014 (Table 2), are independent of macroscopic strain and experimental temperature. The low M indices indicate a lack of crystallographic preferred orientation.

A number of qualitative descriptions of the microstructures of Carrara marble that underwent semi-brittle deformation can be found in previous studies (e.g., Fredrich et al., 1989; Harbord et al., 2023; Olsson & Peng, 1976; Rybacki et al., 2021). In the following, we focus on quantitative characterization of mechanical twins, lattice curvature, and intragranular microfractures.

An example of quantitative characterization of the sample from Run 248 is presented in Figure 5. This sample was deformed to a strain of 4.0% at a temperature of 350°C. The variation of lattice orientation is plotted in the orientation map in Figure 5a. The axial strain accommodated by twins ε_{tYY}, presented in Figure 5b, is variable among grains, with maximum axial strains ranging from −3.6% (i.e., net extension in the direction of the maximum applied load) to +8.9%. Similarly, the GOS map and traced fractures (Figures 5c and 5d, respectively) also illustrate heterogeneous GOS and fracture intensity among grains. The other samples share similar heterogeneity in twin strain, GOS, and microcrack distribution. The compiled displays of all the maps indicate increases of twin strain, GOS, and fracture intensity with increasing macroscopic axial strain (Figures 6–8). In addition, elements of the twin-strain tensor in the direction perpendicular to Y axis, ε_{tXX} and ε_{tZZ} plotted in the Supporting Information S1, were found to be mostly extensional. In the following, we quantitatively examine how these microstructures evolve with increasing macroscopic strain at the three tested temperatures.

3.2.1. Mechanical Twins

The characteristics of the mechanical twins are summarized in Figure 9. During the first 2% axial strain, the twin densities of samples deformed at the three different temperatures increase at similarly steep rates of approximately 51 mm^{-1} per 1% axial strain (Figure 9a). At room temperature, twin density keeps increasing at a similar rate up to 4% axial strain, but saturates between 4% and 8% axial strain. For samples deformed at temperatures of 200°C and 350°C, the accumulation rate significantly decreases after 2% axial strain to approximately 21 mm^{-1} per 1% axial strain, but nonetheless the twin density continues to gradually increase rather than saturating within the strain range of our experiments. The twin densities in samples deformed at a temperature of 200°C are within uncertainty of those in samples deformed at 350°C.

The true twin spacing decreases with increasing axial strain at each temperature (Figure 9b). True twin spacing ranges from approximately 10–30 μm at low strain, and decreases to around 5 μm at 2% strain. From 1% to 4% strain, the twin spacing is slightly less at room temperature than those at 200°C and 350°C. At about 8% strain, the twin spacing data at the three temperatures are approximately the same at about 2.5 μm. The true twin thickness is independent of axial strain, and is generally slightly less at room temperature (around 0.5 μm) than that at higher temperatures (around 0.7 μm) (Figure 9c).

At axial strains ≤2%, the average axial strain accommodated by mechanical twins, ε_{tYY}, is equal to the imposed axial strain across the three temperatures (Figure 9d). However, between 4% and 8% axial strain, ε_{tYY} is typically only approximately half of the imposed strain.

3.2.2. Lattice Curvature

The mean GOS increases with strain at all the tested temperatures, from around 1° at <1% strain to 2.2°–2.6° at 7.5% strain (Figure 10a). The rate of increase in GOS increases with strain at 200°C and 350°C, but is

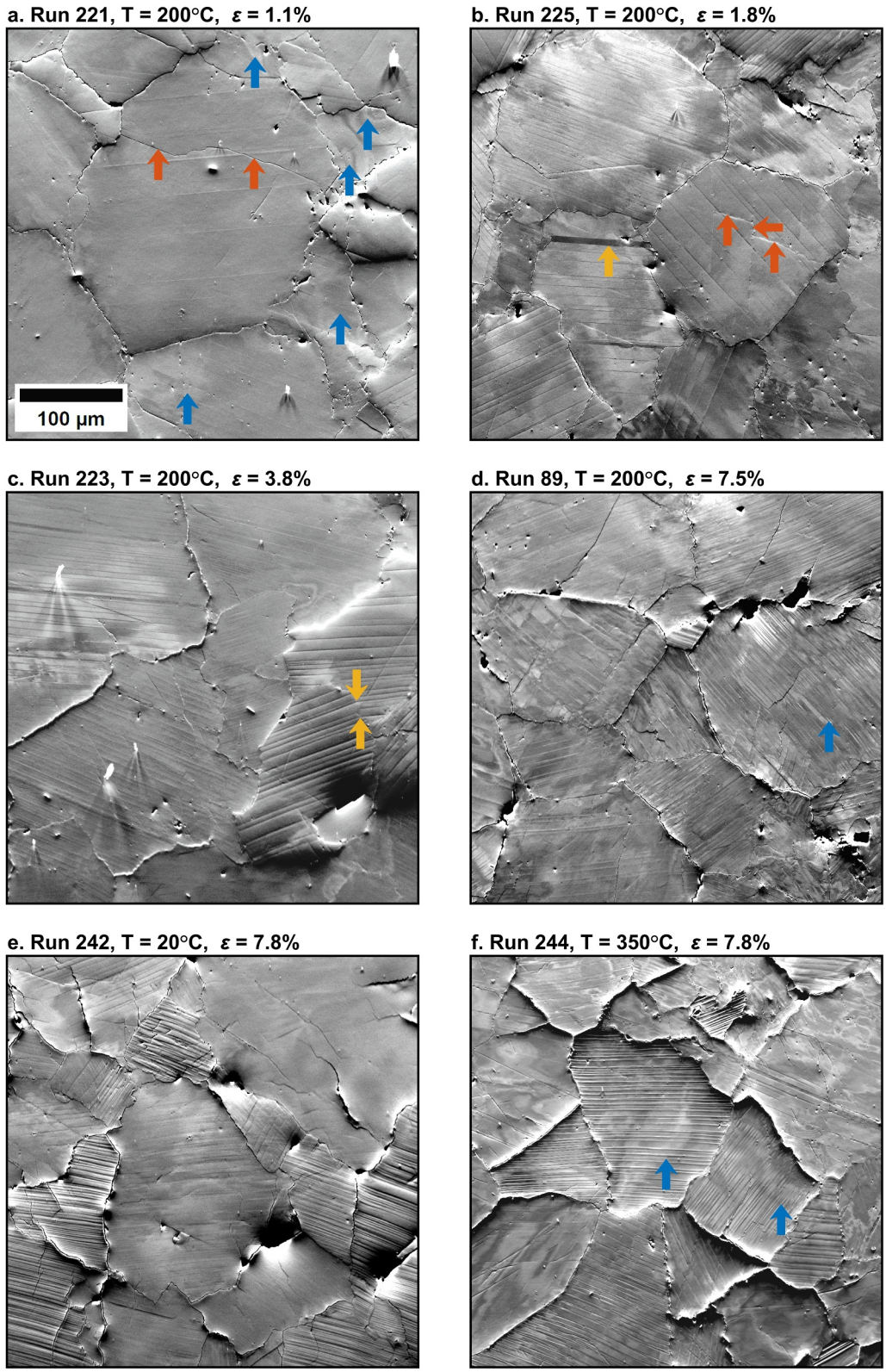

Figure 4.

Table 2
Summary of Microstructural Information

Run	Temperature, °C	ε, %	Grains measured for twin information	Twin density (± uncertainty), mm^{-1}	True twin spacing (± uncertainty), μm	ε_{tYY} (± uncertainty), %	GND density, 10^{12} m^{-2}	Fracture intensity, (± uncertainty) mm^{-1}	*M* index
241	20	0.6	31	50.5 (5.8)	11.6 (1.1)	0.4 (0.3)	0.54	1.7 (0.5)	0.009
239	20	1.0	28	59.1 (6.4)	7.9 (0.9)	1.3 (0.2)	0.57	3.0 (0.6)	0.008
238	20	2.1	30	126.3 (11.8)	4.9 (0.3)	1.9 (0.3)	0.69	7.9 (1.0)	0.008
237	20	4.1	46	264.6 (17.2)	2.5 (0.2)	3.5 (0.5)	0.91	14.9 (2.2)	0.006
242	20	7.8	41	276.8 (20.4)	2.1 (0.2)	4.0 (0.9)	1.29	17.5 (2.8)	0.014
222	200	0.3	34	20.0 (1.9)	30.0 (2.6)	0.4 (0.1)	0.53	1.0 (0.6)	0.014
221	200	1.1	36	62.3 (4.7)	10.7 (0.8)	1.0 (0.2)	0.55	2.7 (1.0)	0.007
225	200	1.8	31	109.9 (11.8)	6.4 (0.6)	1.5 (0.3)	0.56	5.6 (0.9)	0.011
223	200	3.8	43	153.8 (10.8)	4.4 (0.3)	2.0 (0.5)	0.60	6.8 (0.7)	0.011
89	200	7.5	41	200.8 (16.5)	3.3 (0.3)	3.8 (0.7)	1.64	11.6(1.3)	0.006
249	350	0.5	30	33.4 (2.5)	18.4 (1.7)	0.3 (0.1)	0.63	2.0 (0.5)	0.006
247	350	0.8	29	31.0 (4.2)	17.5 (2.3)	0.4 (0.1)	0.55	3.0 (0.5)	0.010
246	350	2.0	30	106.0 (8.3)	6.5 (0.5)	1.9 (0.4)	0.68	5.8 (1.8)	0.014
248	350	4.0	45	138.0 (10.6)	4.7 (0.3)	2.6 (0.6)	0.72	8.0 (1.3)	0.011
244	350	7.8	44	226.0 (15.1)	2.8 (0.2)	4.3 (0.6)	1.59	9.8 (1.7)	0.003

approximately linear at room temperature. The corresponding GND densities also increase with increasing strain (Figure 10b). At the smallest strains of around 0.5%, the GND densities are similar between the three experimental temperatures at around 0.6×10^{12} m^{-2}. At room temperature, the increase is linear up to 1.3×10^{12} m^{-2} at 8% strain. In contrast, at 200°C and 350°C, the increase in GND density is minor up to 4% strain, reaching only around 0.7×10^{12} m^{-2}, but then sharply rises up to 1.6×10^{12} m^{-2} at 7.5% strain.

3.2.3. Intragranular Microfractures

At axial strains ≤2%, fracture intensity exhibits linear increases with strain at rates of approximately 3.5 mm^{-1} per 1% axial strain at all three temperatures in Figure 11a. Above 2% strain, fracture intensities at room temperature are greater than those at the higher temperatures. Specifically, at room temperature, the slope of fracture intensity remains steady between 2% and 4% strain but decreases between 4% and 8% axial strain. At 200°C and 350°C, fracture intensity increases more gradually from 2% to 8% strain than at room temperature, but is similar between these two higher temperatures. From 0.5% to 2% axial strain, more than 50% of the total length of fractures is attributable to cleavage fractures (Figure 11b). This portion is independent of temperature. From 4% to 8% strain, the proportion of cleavage fractures drops below 50%.

The distribution of orientations of the intragranular microcracks is obtained from the orientations of segments between every adjacent two nodes and are presented in 2D rose diagrams with a bin size of 10° (Figure S5 in Supporting Information S1). At room temperature and 200°C, the crack orientations have a rather weak preference for being parallel to the *Y* axis (Run 223 seems to be an exception). At 300°C, the distribution of crack orientations becomes more isotropic. Many cracks are perpendicular to the loading direction. Overall, the microcracks do not exhibit a strong preferred orientation.

Figure 4. Forescattered electron (FSE) images of the tested marble samples. The scale bar in panel (a) is common to all the subfigures. (a) The sample deformed by 1.1% at 200°C from Run 221. Lattice curvature is evident as variation in gray scale, with examples indicated by blue arrows. The straight fractures indicated by orange arrows are possibly cleavage fractures. (b) The sample deformed by 1.8% at 200°C from Run 225. Fractures possibly induced by twinning are indicated by orange arrows. A pre-existing twin is indicated by the yellow arrow. (c) The sample deformed by 3.8% at 200°C from Run 223. The yellow arrows indicate twins potentially induced by twins in neighboring grains. (d) Sample deformed by 7.5% at 200°C from Run 89. The blue arrow points to lattice curvature segmented by twin boundaries. (e) Sample deformed by 7.8% at room temperature from Run 242. (f) Sample deformed by 7.8% at 350°C from Run 244. The blue arrow points to lattice curvature that continues across twin boundaries.

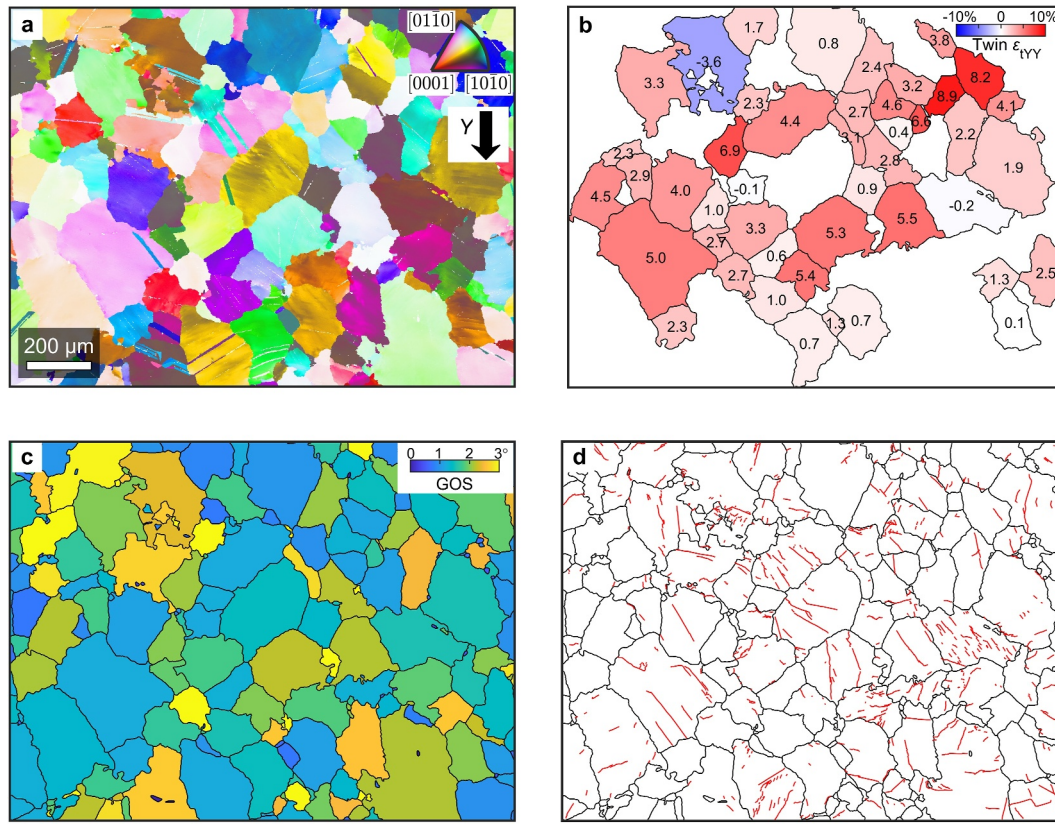

Figure 5. Example of microstructure maps for the sample deformed to a strain of 4.0% at a temperature of 350°C from Run 248. (a) Orientation map from EBSD colored by the inverse pole figure for the *Y* direction (i.e., parallel to the shortening direction indicated by the black arrow). (b) Map of twin strain of selected grains. The positive/negative value of strain is marked on each grain and presented by red/blue colors. (c) Map of grain orientation spread of each grain. (d) Traced intragranular microfractures in red. Reconstructed grain boundaries are in black. The scale bar in subplot (a) is shared with the other three subplots.

4. Discussion

4.1. General Characteristics of Strength Evolution

Several characteristics of the mechanical data from our experiments with the Murrell apparatus are compared to those from previous studies that employed similar experimental conditions (Fredrich et al., 1989; Harbord et al., 2023; Rybacki et al., 2021; Schmid et al., 1980) in Figure 12. In particular, our stress-strain curves are compiled with stress-strain curves from Rybacki et al. (2021) obtained with a Paterson apparatus (Figure 12a). Similar to our experimental conditions, Carrara marble samples reported by Rybacki et al. (2021) were deformed at temperatures of 20–400°C, pressures of 300–400 MPa and strain rates of 1×10^{-6}–5×10^{-5} s^{-1}. Extensive experiments and discussion from Rybacki et al. (2021) indicate that, within these ranges, pressure and strain rate have little influence on the strength of Carrara marble (e.g., Figures 3 and 4 of Rybacki et al., 2021). Our stress-strain curves are broadly in agreement with the measurements from Rybacki et al. (2021). In addition, Figure 12b exhibits clear similarity in stresses at about 1% strain at 20°C, 200°C, 300–400°C.

Our stress measurements at 200°C and 350°C are slightly higher than those from the Paterson apparatus at similar temperatures. The differences in mechanical measurements are associated with differences in experimental setup. The Murrell apparatus uses a two-zone furnace and external load cell, in contrast to the Paterson apparatus with three-zone furnace and internal load cell. Our furnace calibration is in the supplementary material (Figure S2 in Supporting Information S1). The temperature profile exhibits temperatures (200 ± 10°C and 350 ± 25°C) less uniform than those of the Paterson apparatus, but variation of temperature within this range has only modest influence on stress (Figure 12).

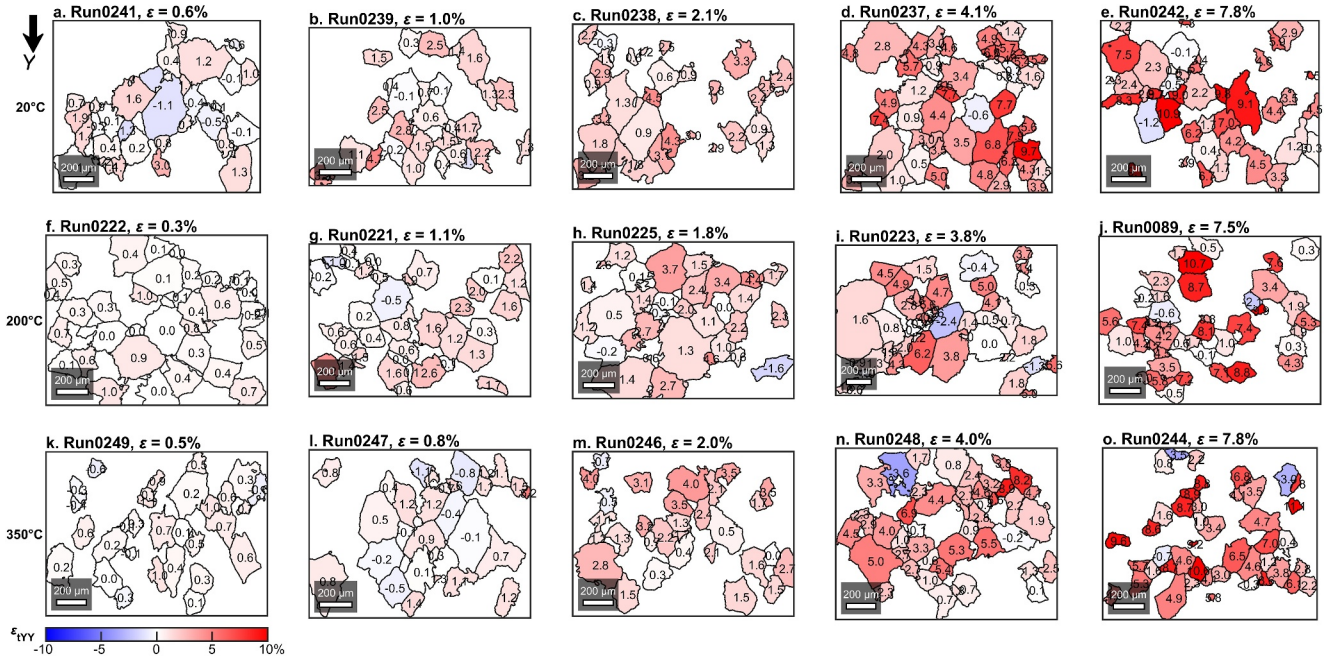

Figure 6. Maps for twin strain ε_{tYY} of selected grains from all the samples deformed at temperatures of 20°C (a–e), 200°C (f–j) or 350°C (k–o). Positive (negative) values of percentage strain for shortening (extension) are marked on each grain and presented as red (blue) colors. From left to right, the macroscopic strain ε increases from 0.5% to 7.5%. The direction of macroscopic loading, Y, is indicated by an arrow. All the subplots share the same color bar.

The load cell of the Murrell apparatus is at ambient pressure and connected to samples at high confining pressure by steel pistons. To correct for the seal friction between steel pistons and the pressure vessel, we need to manually select a hit point (Figure 1) and consider the force at the hit point to be equal to the seal friction. It is not possible to measure the seal friction during deformation of the sample and therefore it is assumed to be constant. In practice, the seal friction can increase with vertical loading due to the horizontal expansion of the steel pistons.

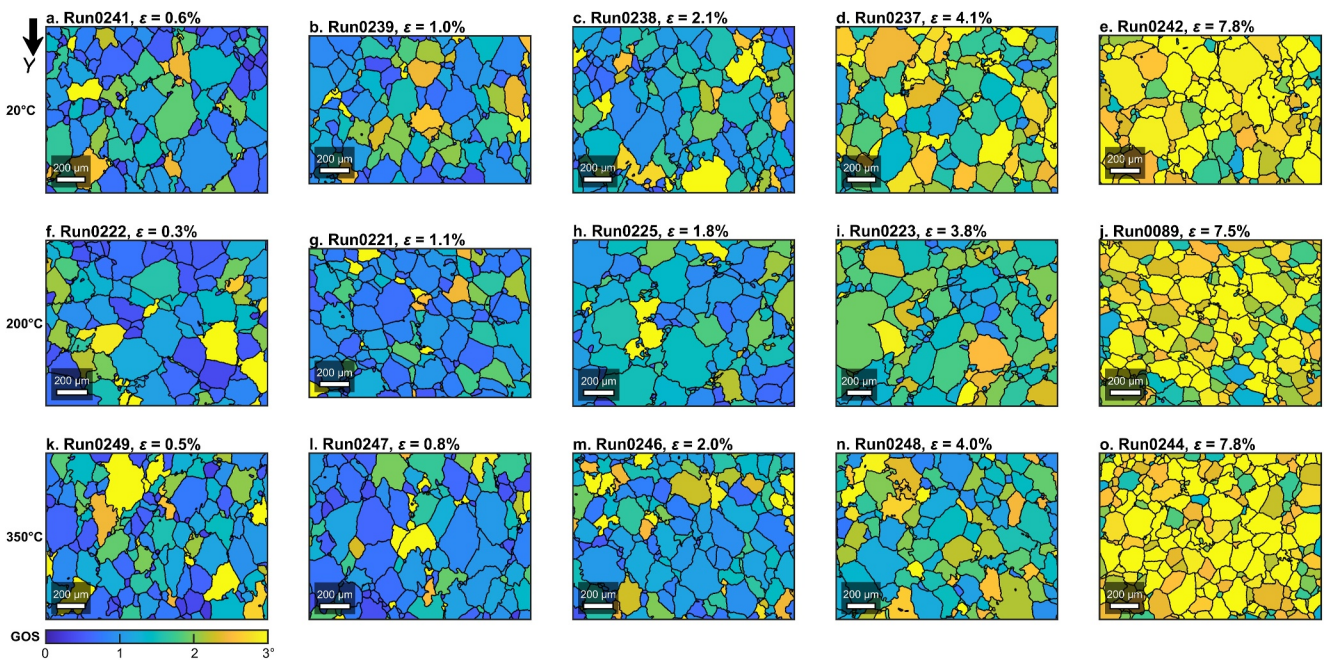

Figure 7. Maps of grain orientation spread from all the samples deformed at temperatures of 20°C (a–e), 200°C (f–j) or 350°C (k–o). The direction of macroscopic loading, Y, is indicated by an arrow. All the subplots share the same color bar.

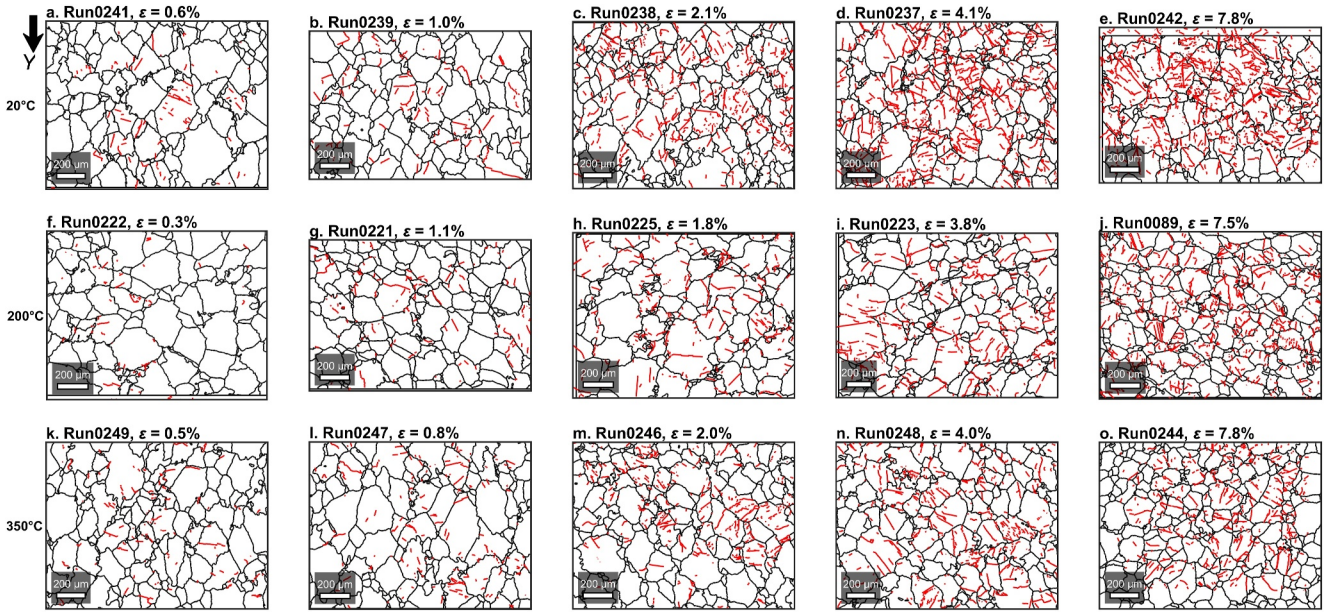

Figure 8. Traced intragranular microfractures (in red) from all the samples deformed at temperatures of 20°C (a–e), 200°C (f–j) or 350°C (k–o). The size of each FSE image for tracing may be modestly mismatched with the size of the corresponding EBSD map, leaving outer edges of EBSD maps within FSE images (e.g., subplots e, f, h, i) or area with no fracture traced (e.g., subplot o). The offset sections were not considered further in the analysis. The direction of macroscopic loading, *Y*, is indicated as arrow.

Nonetheless, the corrected stress-strain curves from the Murrell apparatus agree well with measurement from the Paterson apparatus (Figure 12a).

To analyze the inelastic behaviors of marble undergoing semi-brittle deformation, we consider the evolution of stress from soon after the yield point through subsequent strain hardening (Figure 3a). In particular, we separate the strain-hardening behavior into two stages on the basis of the variation in the rates of hardening and microstructural evolution. From 0% to 2% axial strain, which we term small strain, the hardening modulus from the three sets of experiments drops sharply with axial strain (Figure 3b). Within the range of small strain, the evolution of twin density, true twin spacing and thickness, mean GOS, GND density, and fracture intensity is the same within uncertainty among the three sets of experiments conducted at different temperatures (Figures 9–11). During this stage, axial strain is accommodated almost entirely by mechanical twinning (Figure 9d). The true twin spacing sharply decreases with increasing strain (Figure 9b), and GND density remains low (Figure 10b).

Beyond 2% strain, which we term intermediate strain, the hardening modulus decreases modestly with further strain (Figure 3b). At intermediate strain, the samples from all three sets of experiments start to develop more lattice curvature, observed as increases in estimated GND density (Figure 10b), whereas true twin spacing decreases more modestly with axial strain than it does at small strain (Figure 9b). In particular, at intermediate strain, the samples deformed at room temperature have greater twin density (Figure 9a), lesser GND density (Figure 10b), and greater fracture intensity (Figure 11), relative to the samples deformed at 200°C and 350°C. In contrast, the measurements of these microstructural elements are within uncertainty of each other between the samples deformed at 200°C and 350°C (hereafter referred to as high experimental temperatures).

4.2. Microstructural Evolution During Semi-Brittle Deformation

The microstructural analyses of this study are at a scale of tens of grains or 1 mm^2. Although each sample with a mean grain size of about 200 μm contains about 1×10^6 grains, the representativeness of our measurements is supported by the following points. First, there is no visible localized deformation at the macroscopic scale. Second, the statistical uncertainties are relatively small, compared with the absolute values of twin information (except for twin thickness) and intragranular fracture intensity. Third, gridded maps of split Carrara marble samples deformed at 400°C from Xu and Evans (2010) and Quintanilla-Terminel and Evans (2016) show a reasonable strain homogeneity at the scale of tens of grains or 1 mm^2. As the general operation of three major

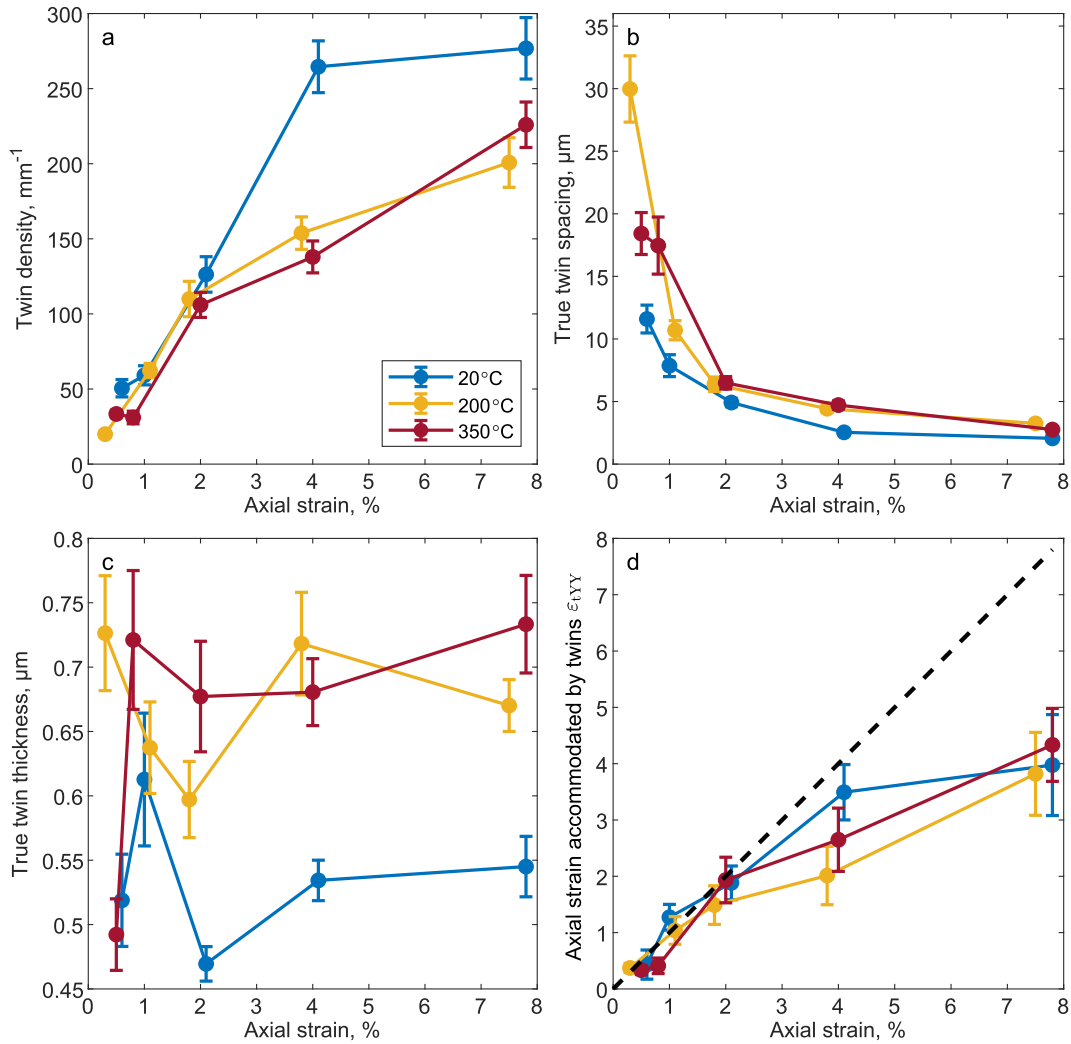

Figure 9. (a) Twin density of each tested sample, calculated as the total number of measured twins over the total length of measured grain widths. (b) Average true twin spacing. The data here and in subplot (c) are corrected by the inclination angle β for each set of twins. For data above 4% axial strain, the error bar covers a range around, or smaller than, the diameter of the markers. (c) Average true twin thickness. (d) Component of the twin-strain tensor parallel to the loading direction. The error bars are uncertainties of measurements introduced in Section 2.3.1.

types of microstructural activities (i.e., twinning, dislocation glide, microfracturing) is similar for marble deformed at room temperature to 400°C, the scale assessment of strain homogeneity from Quintanilla-Terminel and Evans (2016) is likely also broadly characteristic of our samples. In addition, our microstructural observations were always conducted at the same location, the center of the deformed samples, which ensures consistent methodology for microstructural characterization.

The microstructural evolution of Carrara marble during semi-brittle deformation can be inferred from the results of our mechanical testing and microstructural characterization, as follows. During the initial increment of loading, the randomly oriented grains undergo different elastic strains due to their anisotropic stiffness. With loading progressively increased, this elastic anisotropy causes the stress and elastic strain fields to become increasingly heterogeneous among adjacent grains.

Once the stress locally exceeds a critical stress for twinning, dislocation glide, or microcracking, permanent deformation occurs and partially relaxes the intergranular stress heterogeneity resulting from elastic anisotropy. As the critical resolved shear stress (CRSS) to initiate twinning is low (Figure 12b), twinning is the primary deformation mechanism even before 0.5% strain. Because calcite only has three possible *e* twin systems, the

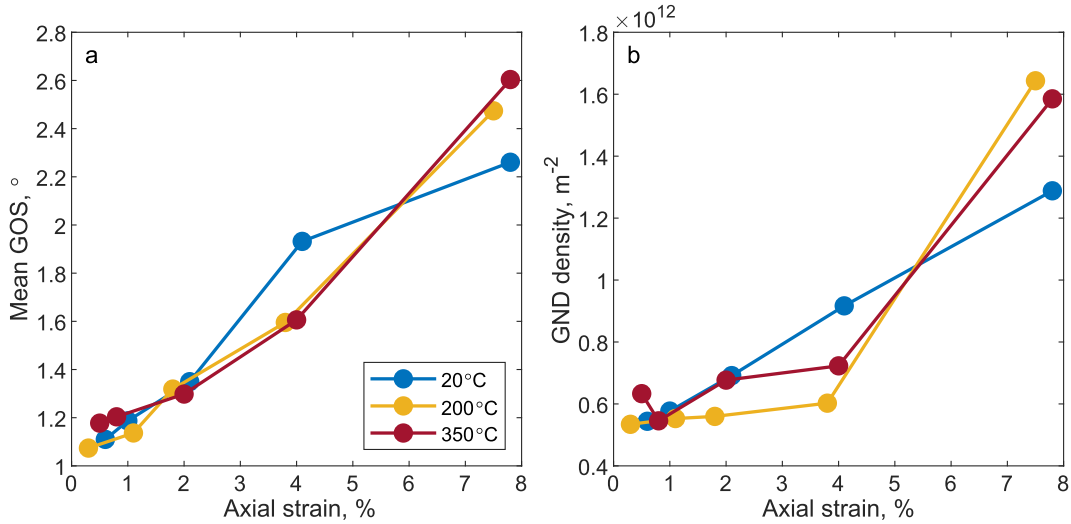

Figure 10. (a) Mean grain orientation spread (GOS) against axial strain. (b) geometrically necessary dislocations density, estimated from GOS and grain size, against axial strain.

intergranular heterogeneity in strain cannot be fully accommodated by twins alone as, according to the von Mises criterion (von Mises, 1928), five independent slip/twin systems are required to allow sufficient strain components in the absence of other significant processes to maintain strain compatibility. In addition, the process of twinning, with the associated contribution to the strain tensor depending on crystal orientation, would introduce further intergranular interaction. Due to these effects, stress differences between grains cannot be completely relieved by twins, so heterogeneity in elastic strain partially remains and the material strain hardens.

In the stage of intermediate macroscopic strain, stress concentrations induced by anisotropic elasticity and twinning exceed the critical stress to initiate dislocation glide and/or intragranular microfracturing. Compared with twins that typically extend across grains, individual dislocations with the width of Burgers vectors permit more strain heterogeneity within grains.

Under our experimental conditions, differential stress remains consistently less than the confining pressure of 400 MPa. According to Goetze's criterion (Kohlstedt et al., 1995), such a condition is unfavorable for development of fractures. However, prior experiments conducted at confining pressures equal to or exceeding 400 MPa have demonstrated three key phenomena: (a) minimal but non-zero pressure dependence of sample strength (e.g.,

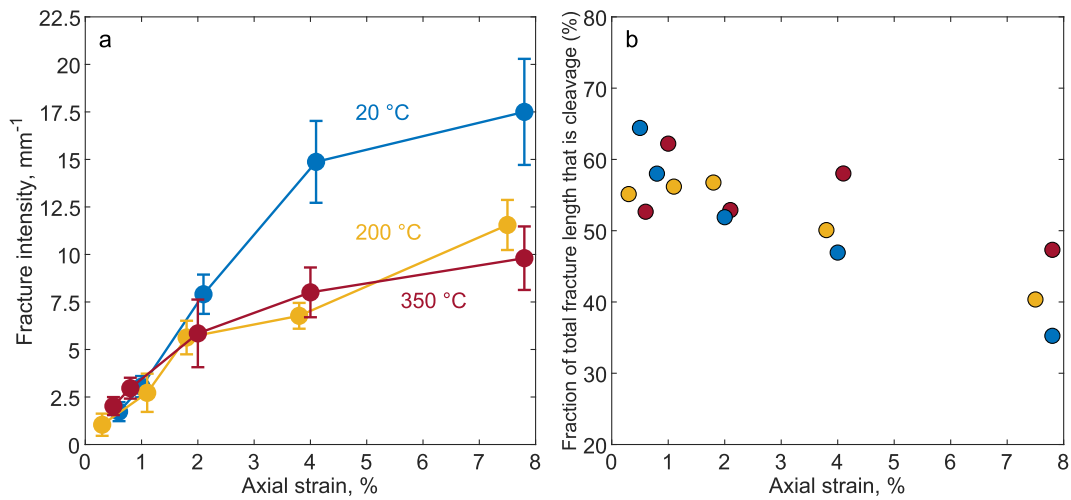

Figure 11. (a) Fracture intensity against axial strain at different temperatures. (b) Fraction of total fracture length that is cleavage against axial strain. The colors of markers represent temperatures, shared in the two subplots.

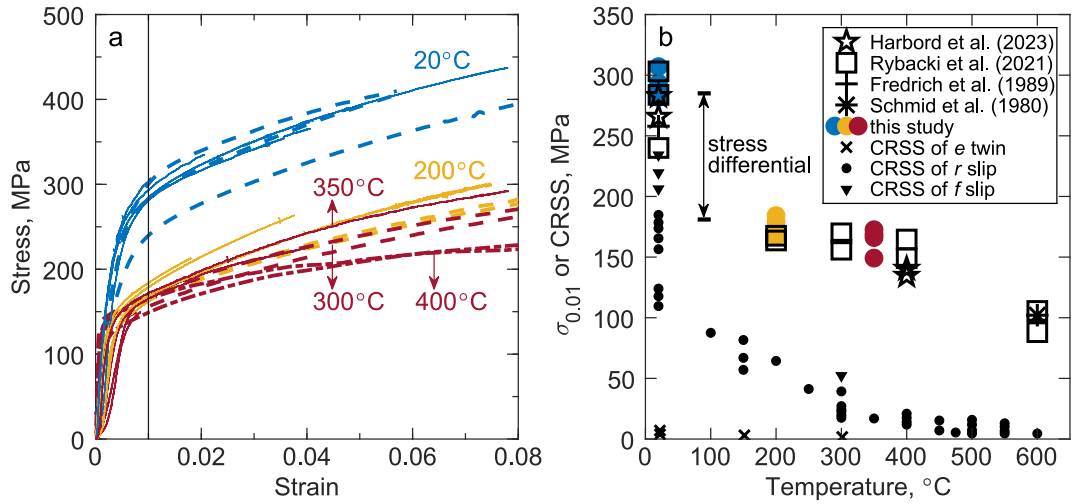

Figure 12. (a) Mechanical data from previous experiments on Carrara marble at pressures (300–400 MPa) and strain rates (1×10^{-6}–5×10^{-5} s^{-1}) (broken lines, reproduced from Rybacki et al., 2021) and those from our experiments (solid lines). (b) Macroscopic stress at 1% axial strain, $\sigma_{0.01}$, at the same range of pressures and strain rates as the conditions of subplot a, from this and previous studies (Fredrich et al., 1989; Harbord et al., 2023; Rybacki et al., 2021; Schmid et al., 1980) along with the critical resolved shear stresses (CRSS) for *e* twinning, $r\{10\bar{1}4\}\langle\bar{2}021\rangle^{\pm}$ slip, and $f\{\bar{1}012\}\langle 2\bar{2}01\rangle^{-}$ slip reproduced from Figure 10 of de Bresser and Spiers (1997, and references therein).

Figures 2 and 3a in Rybacki et al., 2021), (b) syn-deformation reduction of ultrasonic wave speed and (c) strong intragranular stress heterogeneity revealed by high-angular resolution EBSD (Harbord et al., 2023). While post-deformation processes such as quenching and decompression during unloading can induce fracturing in marble (Edmond & Paterson, 1972; Harbord et al., 2023), the previous observations suggest that a portion of the fractures traced in our experiments must have originated during active deformation rather than post-mortem relaxation.

At axial strain larger than 2%, by which point twins, intragranular fractures and GND density have adequately developed, no grains simultaneously have high GND density, high fracture intensity and high engineering shear strain due to twinning (Figures 13a–13c). Among the 41–44 grains selected for each measurement, only a few grains have high quantities in any two measurements at each temperature. In most cases, those grains with high GND density (> 80th percentile) do not have high fracture intensity or high twinning strain. The low probability for co-occurrence of any two high values of these microstructural quantities (Figures 13a–13c) suggests that the deformation in some of the measured grains may be selectively dominated by a single deformation mechanism

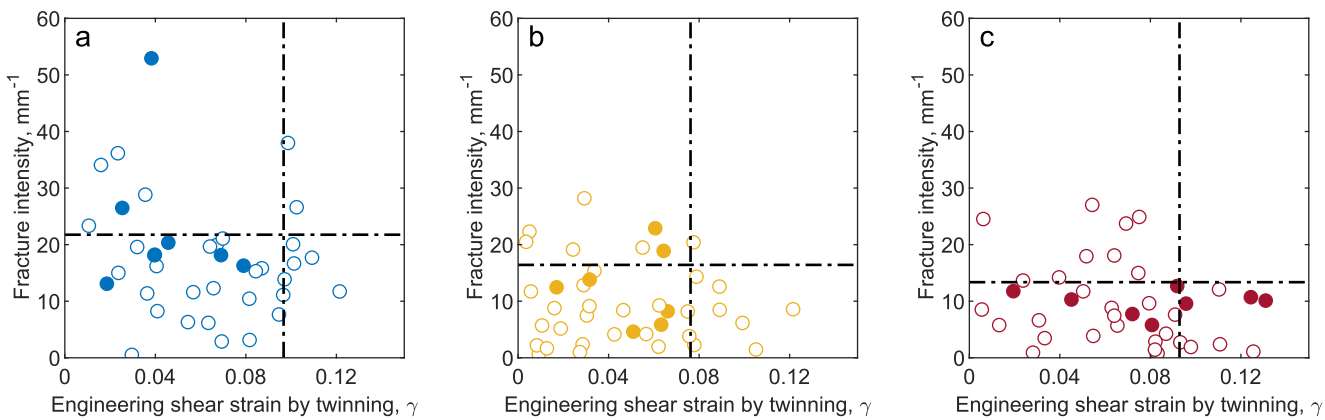

Figure 13. Fracture intensity against engineering shear strain γ accommodated by twins (Equation 2) of each grain selected for twin characterization at about 7.5% macroscopic strain at panel (a) room temperature, (b) 200°C, (c) 350°C. The intercepts of the dashed lines with either the horizontal or vertical axis correspond to the 80th percentile for the respective type of microstructural measurement. Markers in the top right area confined by broken lines are thus considered as grains with two simultaneously high microstructural measurements. The solid markers represent grains with geometrically necessary dislocations (GND) density higher than 80th percentile, and open markers are grains with GND density lower than that.

(i.e., fracturing, dislocation glide, or twinning). Most grains underwent moderate levels of two or three deformation mechanisms to accommodate local strain.

The relative displacement between grains was not possible to evaluate with our approach. Nonetheless, micro-scale strain maps from Carrara marble samples deformed as split cylinders revealed that local strains along grain boundaries are associated with twinned grains at temperatures of 400°C and 500°C (Section 3.5 in Quintanilla-Terminel & Evans, 2016). This observation suggests that grain-boundary sliding at low temperatures must occur, but not as a pervasive process to accommodate strain. Instead, the relative displacement/rotation between grains at low temperatures is specifically related to intergranular interaction induced by twinning.

4.3. Stress Differential Between Room Temperature and High Experimental Temperatures

An obvious feature of the stress data is that the strength of Carrara marble at any given finite strain is substantially greater at room temperature than at 200°C and 350°C (Figure 12a). This stress differential appears at the onset of inelastic deformation and remains almost constant, around 120 MPa, up to 8% axial strain. Similar measurements have been obtained under similar confining pressures of 300–400 MPa in the previous studies compiled in Figure 12b (Fredrich et al., 1989; Harbord et al., 2023; Rybacki et al., 2021; Schmid et al., 1980). As microstructures of samples deformed at small strain do not significantly differ at the three experimental temperatures, the strength difference between the measurements at room temperature and high experimental temperatures cannot be attributed to a shift in the relative activity of the three major deformation mechanisms (i.e., twinning, fracturing, and dislocation glide), but rather to the temperature sensitivity of the strength-limiting mechanism(s). Given that fracture toughness is mostly insensitive to temperature (e.g., Al-Shayea et al., 2000; Chandler et al., 2017), the contribution of fractures to the stress differential is likely negligible. In addition, the critical resolved shear stress of *e* twinning in single crystals is as low as 10 MPa at room temperature and decreases to about 5 MPa at high experimental temperatures (de Bresser & Spiers, 1997), and therefore this weak temperature dependence is also insufficient to account for the stress differential. Accordingly, the temperature dependence of the onset of inelasticity can only be attributed to dislocation activity. The CRSSs for slip systems in single crystals are compiled in Figure 10 of de Bresser and Spiers (1997) and reproduced in Figure 12a. The CRSS of the easy slip system, *r* slip $\{10\bar{1}4\}\langle\bar{2}021\rangle$, exhibits a nonlinear dependence on temperature, decreasing from approximately 150 MPa at room temperature to about 50 MPa at 200°C, but only decreasing to about 20 MPa at 350°C. As such, the temperature dependencies of the strengths of single crystals and Carrara marble are similar (Figure 12b), whilst the absolute strengths differ due to additional factors, such as to differences in average resolved shear stress (i.e., due to differences in average Schmid factor) and differences in grain size (Harbord et al., 2023).

The inference that stress at the onset of inelastic deformation is controlled by dislocation glide needs to be reconciled with the observation that, in calcite aggregates, twinning is the primary mechanism to accommodate axial strain at small strain (Figure 9d). However, twinning, as inhomogeneous deformation at grain scale (Figure 2d), would induce intergranular stress heterogeneity. For calcite grains oriented unfavorably for twinning and fracturing, the accumulated intergranular stress would induce *r* and *f* slip. Whilst dislocation glide is not the dominant strain accommodating mechanism at small strain, dislocation activity can be inferred from orientation maps and FSE images. For example, local lattice curvature is present in samples deformed to a strain of 1% (Figure 4). These grains with lattice curvature are possibly stronger than other grains permanently deformed by fracturing or twinning, and therefore dislocation glide in these grains may have controlled the macroscopic strength of the samples.

4.4. Strain Hardening

4.4.1. Strain Hardening by Hindering Dislocation Glide

In this section, we consider the role of dislocation glide in post-yield strength evolution. Dislocation glide can be hindered by interactions between dislocations and obstacles (e.g., other dislocations, twin boundaries) that can increase in intensity with macroscopic strain (Taylor, 1934). Furthermore, the expansion of a dislocation loop is resisted by line tension as it emanates between the two pinning points of a Frank-Read source (Weertman & Weertman, 1971, p. 125). These effects generate an internal stress σ_i that hinders dislocation glide and generally has the form

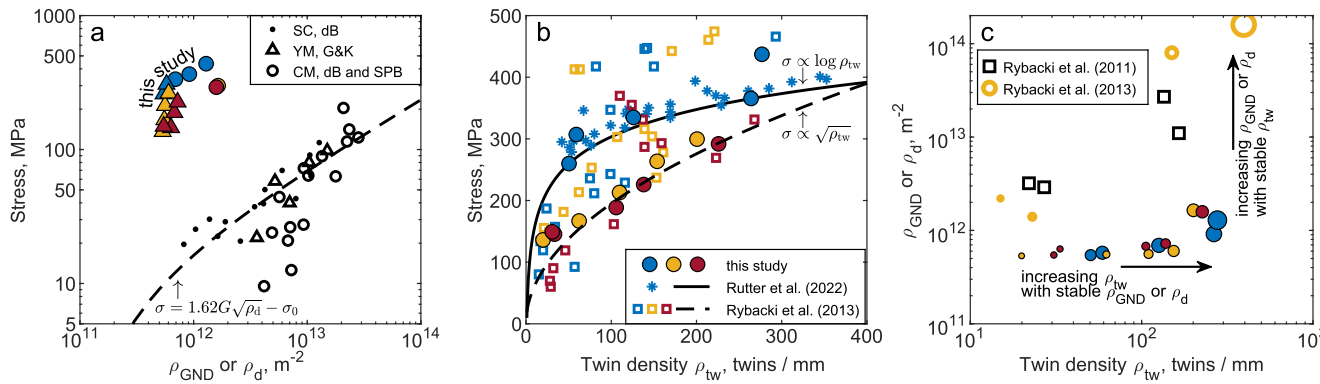

Figure 14. (a) Differential stress against geometrically necessary dislocation density from this study and total dislocation density of calcite single crystals (SC), Yule marble (YM), and Carrara marble (CM) from previous studies. The data and fitting dashed line from de Bresser (1996) (dB) were obtained from uniaxial deformation of single-crystal calcite in the [40$\bar{4}$1] direction at temperatures of 550–800°C. σ_0 in the function of the dashed line is a stress constant without a definitive theoretical foundation (de Bresser, 1996). The Yule marble was deformed by Heard and Raleigh (1972) at temperatures of 500–800°C followed by microstructural characterization by Goetze and Kohlstedt (1977) (G&K). The Carrara marble was deformed at temperatures of 600–1,050°C and examined by Schmid et al. (1980) (SPB) and de Bresser (1996). (b) Differential stress against twin density from deformation experiments on Carrara marble in similar temperature ranges. Blue, yellow and red respectively represent temperature ranges of 20–100°C, 200–250°C, and 300–400°C. Data of Rybacki et al. (2013) are from confining pressures of 100–400 MPa and strain rates of 1×10^{-3} s^{-1} to 1×10^{-6} s^{-1} (including samples CM22, CM25, CM34, CM40, CM41, and CM46 in compression, and samples CMDB1, CMDB6, and CMDB8 in torsion with shear stress converted to equivalent differential stress). The broken line is from Equation 6 of Rybacki et al. (2013). The solid line is Equation 2 of Rutter et al. (2022) fitted to data from a dog-bone shaped sample deformed at a confining pressure of 225 MPa and at a nominal axial strain rate of 4×10^{-5} s^{-1} (c) ρ_{GND} or ρ_d against twin density. Color-filled circles are from this study. Black squares are from calcite veins in drill core from the San Andreas Fault (Rybacki et al., 2011). Yellow open circle are from CMDB5 in Rybacki et al. (2013), deformed in torsion at a temperature of 150°C and confining pressure of 400 MPa. The sizes of all the circles are proportionate to the magnitude of equivalent differential stress.

$$\sigma_i \propto \frac{Gb}{\lambda}, \tag{10}$$

where G is the shear modulus, b is the magnitude of Burgers vector, and λ is the average spacing of dislocations or their pinning points. With plastic strain, λ is expected to decrease due to increasing dislocation density (Kocks & Mecking, 2003). Therefore, in studies on mechanical properties of metals (e.g., Bouaziz & Guelton, 2001; Mecking & Kocks, 1981) and silicate minerals, such as olivine, quartz, and plagioclase feldspar (Breithaupt et al., 2023; Kohlstedt & Weathers, 1980; Thom et al., 2022), λ is usually approximated as the square root of dislocation density (ρ_d), following

$$\sigma_i = \alpha G b \sqrt{\rho_d}, \tag{11}$$

known as the Taylor equation, where α is a geometric coefficient (Taylor, 1934). Calcite single crystals also exhibit this relationship, as demonstrated by the σ-ρ_d data from de Bresser (1996) presented in Figure 14a. These mechanical data were obtained by uniaxial compression in the [40$\bar{4}$1] direction at temperatures of 550–800°C and ambient pressure. Dislocation density was directly measured as the number of dislocations per unit area by transmission electron microscopy.

Our measurement of GND density is an indirect measurement of dislocation density. We note that apparent GND densities are inversely proportional to the length scale over which they are measured for two reasons (Wallis et al., 2016). First, the noise floor in estimates of GND density decreases with increasing length scale as the effect of noise in the lattice rotations becomes proportionately less. Second, a greater fraction of the total dislocation density will become statistically stored dislocations with increasing length scale as the curvature produced by each dislocation becomes more likely to be canceled by a dislocation with a Burgers vector of opposite sign. As our estimates of ρ_{GND} were computed over the length scale of the grain size (i.e., the largest meaningful length scale) they likely provide a lower bound on the total dislocation density in each sample.

A comparison between the GND densities from our study and the total dislocation densities in single crystals measured by de Bresser (1996) reveals that our samples deformed to high stresses (plotted as filled circles in

Figure 14a) exhibit a similar proportionality between σ and $\sqrt{\rho_{GND}}$ as do the single crystals. This similarity suggests an important role of dislocation interactions in hindering dislocation glide during strain hardening at intermediate strain.

Our samples deformed to low final stresses (plotted as filled triangles in Figure 14a) exhibit a different relationship between σ and ρ_{GND}, whereby stress increases with little change in ρ_{GND} (Figure 14a). This effect is mirrored in tests on coarse-grained marble deformed to steady state at temperatures greater than 500°C (Figure 14a). In these previous data, σ increases rapidly with relatively little change in ρ_d at low stress and only follows $\sigma \propto \sqrt{\rho_d}$ at relatively high stresses (Figure 14a) (de Bresser, 1996; Goetze & Kohlstedt, 1977; Schmid et al., 1980). After evaluating the influence from recovery kinetics and experimental unloading/cooling effects, de Bresser (1996) proposed that this effect arises due to strain incompatibility at grain boundaries in polycrystals, which is absent in single crystals. The strain incompatibility between grains would produce GND near grain boundaries to maintain compatible deformation of the bulk sample. Based on the assumption that each GND contributes less hardening than does a SSD, de Bresser (1996) proposed a non-linear relation between stress and $\sqrt{\rho_d}$ for calcite polycrystals (his Equations 12 and 17). However, the designation of a dislocation as a GND or SSD is an observational description based on whether or not it generates net lattice curvature over the length scale of interest defined by the observer and does not in itself denote a fundamental change in the physical properties or associated processes of the dislocation, at least not without further assumptions.

Alternative to the explanation proposed by de Bresser (1996) for the disparity in σ-ρ_d relation between single crystals and polycrystals, increases in stress due to grain boundaries and twin boundaries hindering dislocation glide is a potential explanation. In de Bresser's experiments, the calcite single crystals were uniaxially compressed along $[40\bar{4}1]$, which leads to Schmid factors for *e* twins of 0 or 0.12, much lower than the Schmid factors for *r* and *f* slip (Table 1 in de Bresser & Spiers, 1990), while the CRSSs for *e* twinning, and *r* and *f* slip are similar at high temperature >500°C (Figure 10 in de Bresser & Spiers, 1997). Therefore, twins are less abundant in these single crystals (e.g., Figure 6a in de Bresser & Spiers, 1990) than in marble (e.g., Figures 6a–6c in de Bresser et al., 2005; Figures 8g and 8h in Rybacki et al., 2021). Twins with low CRSS can be strongly developed at low macroscopic stress, and correspondingly, marble samples would harden as dislocation glide may be hindered by twin boundaries. Accordingly, twin density may serve as a secondary variable that reduces the apparent sensitivity of the macroscopic stress to ρ_d in the low stress regime (Figure 14a).

Twin density linearly increases with stress in our samples (Figure 14b). From previous mechanical testing on Carrara marble, an empirical relation of the form $\sigma \propto \log(\rho_{tw})$ was proposed by Rutter et al. (2022), while similarly, Rybacki et al. (2013) suggested the relation to be $\sigma \propto \sqrt{\rho_{tw}}$ (Figure 14b). Although the two proposed relations cannot be distinguished based on the scattered measurements (Figure 14b), a correlation between stress and twin density has been generally accepted (e.g., Amrouch et al., 2010; Lacombe et al., 1992; Seybold et al., 2023).

Microstructural observations (i.e., EBSD, high-angular resolution EBSD, and FSE data) indicate that some twin boundaries in Carrara marble do impede dislocation glide in instances where they have low transmission factors based on the orientation relationships between the applied stress, slip system, and twin system (Harbord et al., 2023). Thus, for our measurements, the increase of stress at small strain with little increase of ρ_{GND} is plausibly attributable to an increase in the spatial density of twin boundaries, which hinder dislocation glide, similar to the previous observations made at steady state (Figure 14a) (Rybacki et al., 2021).

Overall, the relationships among our microstructural and mechanical data suggest that the strain hardening in marble is likely to be controlled by increasing resistance to dislocation glide, initially with twin boundaries as the main barriers that are increasing in abundance, progressively complemented by dislocation-dislocation interactions. At small strain, we observed increasing ρ_{tw} with stable ρ_{GND}. At intermediate strain, ρ_{tw} tends to become stable while ρ_{GND} significantly increases. The measurements of ρ_{tw} and ρ_d on the same samples from calcite veins in natural faults (Rybacki et al., 2011) and experiments (CMDB5 in Rybacki et al., 2013) generally follow this pattern (indicated by arrows in Figure 14c).

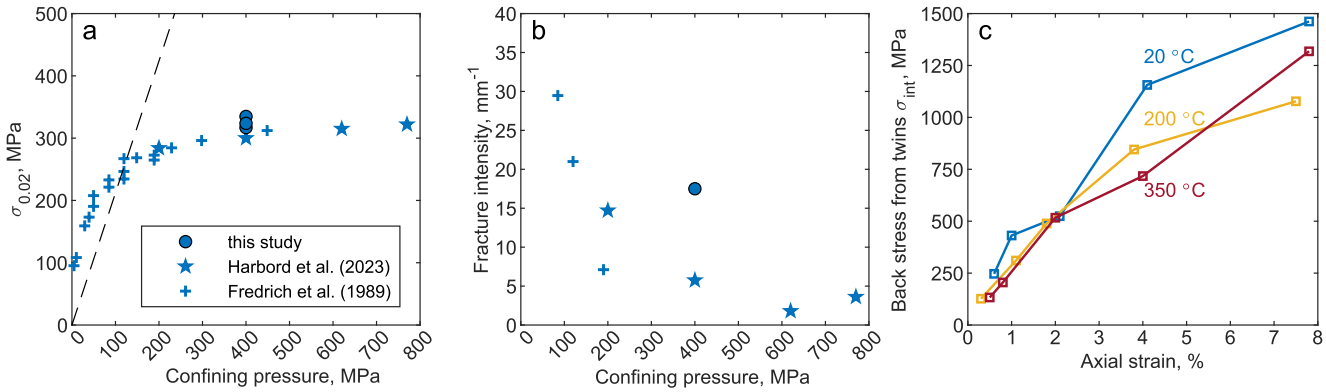

Figure 15. (a) Differential stress at 2% axial strain ($\sigma_{0.02}$) for Carrara marble deformed at room temperature and different pressures. The broken line represents the differential stress to allow frictional sliding on an optimally oriented fault with a frictional coefficient of 0.6, reproduced from Equations 4 and 5 from Rybacki et al. (2021). (b) Fracture intensity of Carrara marble deformed at room temperature and different confining pressures, obtained by the line-intercept method (Fredrich et al., 1989; Harbord et al., 2023) and tracing method (this study). The data from Fredrich et al. (1989) are from samples deformed to strains of 4.6%–5.5%. The data from this study and Harbord et al. (2023) are from samples deformed to strains of about 7.5%. The line-intercept method of Harbord et al. (2023) is different from our fracture-tracing approach, leading to discrepancies in results at 400 MPa. (c) Intergranular back stress from twins from Equation 12.

4.4.2. Dilatancy and Frictional Slip

Our microstructural observations indicate the presence of opening mode microcracks, which should contribute to dilatancy and may thus impact the overall resistance to deformation by contributing to the energy balance of the deformation experiments (Edmond & Paterson, 1972). We could not measure dilatancy in our experimental setup, but previous work on Carrara marble shows that dilatancy, although non-zero, has a negligible contribution to work dissipation compared to that of differential stress and axial strain at 300–400 MPa confining pressure (Edmond & Paterson, 1972; Fredrich et al., 1989). Therefore, the contribution of dilatancy to the overall resistance to deformation and hardening is likely insignificant.

Plausibly, the strain-hardening behavior might also be attributable to frictional slip on shear cracks during compressive loading under confinement. At sufficiently high pressures, any pre-existing cracks are mostly closed, inferred from ultrasonic measurements on pressurized rock samples (Birch & Bancroft, 1938; Walsh, 1966). Thus, before reaching the yield point, loading induces a linear elastic response determined by the intrinsic Young's modulus of the intact solid (Walsh, 1965). As stress and strain increase, the behavior deviates from linearity (e.g., Figure 1b). If crystal-plastic behavior were not involved, the non-linearity could be explained by frictional displacement on pre-existing microfractures and observed as apparent strain hardening after yielding (e.g., David et al., 2020; Walsh, 1965). However, in experiments at confining pressures of 400 MPa and above, the macroscopic strength of marble (Figure 15a) and the fracture intensity of samples (Figure 15b) (Fredrich et al., 1989; Harbord et al., 2023) exhibit minimal pressure dependence. In addition, the fractures are usually intragranular and do not extend across an entire grain (Fredrich et al., 1989, also Figure 4 of this study). This observation is consistent with the analytical modeling in Bernabé and Peč (2024) that shear stresses around isolated pores can only induce sliding localized in the vicinity of the pores at high confining pressure. Furthermore, the differential stress to drive frictional sliding on an optimally oriented fault (broken line in Figure 15a) is significantly higher than our stresses. These observations suggest that frictional slip on fractures is mostly limited in our samples, and thus cannot contribute much to the strain-hardening behavior.

4.4.3. Intergranular Back Stress at Twin Tips

The pervasive twinning, as an heterogeneous deformation process at the grain scale (Figure 2c), induces geometric complications at grain boundaries (e.g., Burkhard, 1993). If a twinned grain is between two elastic grains with no imperfections such as twins or fractures, any intergranular back stress (σ_{int}), induced by strain incompatibility at twin tips, might also contribute to strain hardening. The calculation of σ_{int} has been proposed by Mitchell and Hirth (1991) as

$$\sigma_{\text{int}} = \frac{y_0 \varepsilon_{\text{t0}} G_{\text{VRH}}}{d_{\text{twsp}}}, \tag{12}$$

where y_0 is the halved true width of twins, d_{twsp} is the true twin spacing and ε_{t0} is the engineering twin strain for a single twin. The stress computed by Equation 12 is an upper bound as linear-elastic behavior is assumed for the material surrounding the twins.

The resulting estimates of σ_{int} are similar for all tested temperatures (Figure 15c). The stress estimates are least at around 250 MPa at 0.5% strain, and increase up to 1–1.5 GPa at 7.5%–8% strain. Such high estimated stresses indicate that twinning in one grain leads to strong stress concentrations in adjacent grains. However, once the intergranular stress is beyond a critical stress, the stress concentrations are prevented from increasing further by intragranular flow (i.e., twinning or dislocation glide) or fracturing in the neighboring grains. Accordingly, intragranular mechanisms, rather than intergranular back stress at twin tips, dominate the macroscopic hardening behavior.

4.4.4. Other Possible Hardening or Softening Mechanisms

Alongside dislocation glide hindered by increasing obstacles and limited frictional sliding on shear cracks, many other intragranular processes might also have some influence on the strength of deformed marble. From fcc alloys, it has been reported that the CRSS to induce twins is increased by intersection of different twin sets in fcc alloys (Alkan et al., 2018; Bönisch et al., 2018). Furthermore, the strength of marble undergoing semi-brittle deformation can be influenced by complicated direct interactions between fractures and dislocations. Dislocations can be generated at stress concentrations at fracture tips (e.g., Anderson & Rice, 1986), which facilitates plastic deformation at relatively low macroscopic stress and is, in this respect, a softening process. However, any resulting increase in the intensity of dislocation interactions or shielding of stress concentrations at the fracture tips could also contribute a hardening effect (Section 7.3 in Lawn, 1993). In addition, the strength of tested samples may be indirectly influenced by dynamic recovery processes, including cross slip (de Bresser, 2002), annihilation (Nes, 1997), or dislocation removal at new free surfaces created by fracturing (Chapter 9 in Brantut, 2025; Caillard & Martin, 2003). The aforementioned mechanisms in this subsection are difficult to test, because they do not have a resolvable mechanical or microstructural signature that we can identify.

It is most likely that dislocation glide hindered by increasing obstacles dominates the observed strain hardening in marble. This interpretation is supported by the results of mechanical testing and microstructural observations. First, the stress differential between room temperature and high experimental temperatures, which is first apparent at the onset of inelasticity and is interpreted to be associated with dislocation glide, remains nearly constant with strain (Section 4.3). Second, the temperature independence of hardening rate is a known characteristic of hardening by dislocation interactions (Hansen et al., 2019; Kocks & Mecking, 2003). Third, the relationship between the development of twin density and that of GND density with increasing strain and macroscopic stress is consistent with them playing a coupled role in controlling the strength evolution (Section 4.4.1).

4.5. A Phenomenological Model for Ductile Semi-Brittle Deformation of Marble

We develop a phenomenological model based on the assumption that strain hardening is attributed to dislocation glide hindered by twin boundaries and dislocation interactions. As indicated by Equation 10, the shortening of length scale λ for dislocation glide is key in this process. Following the discussion in Section 4.4.1, interactions of dislocations with other dislocations and twin boundaries (and grain boundaries) can jointly contribute to obstruction of dislocation glide. As the interaction among dislocations and interaction between dislocations and twin/grain boundaries cannot be physically isolated here, λ in Equation 10 is approximated as the harmonic average of the distances between dislocations and the distances between twin boundaries (Breithaupt et al., 2023). Thus, the Taylor relation can be extended as

$$\sigma = k_{\text{C}} \tau_{\text{C0}} + \frac{k_{\text{tw}} G b}{d_{\text{twsp}}} + k_{\text{GND}} G b \sqrt{\rho_{\text{GND}}} \tag{13}$$

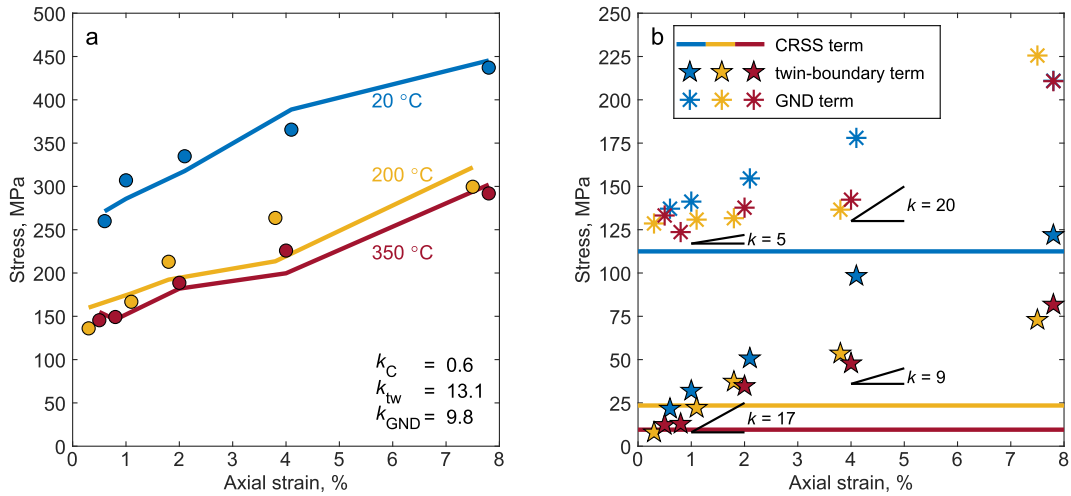

Figure 16. (a) Linear least-square inversion results (lines) with experimental measurements of stress for the 15 samples. (b) Contribution of the four terms in Equation 13, the extended Taylor relation, to the modeled strength. The datum for the geometrically necessary dislocations (GND) term at the greatest strain at room temperature is overlapped by the datum for 350°C. k indicates the slope of stress-strain data for twin-boundary term or GND term in the early or late stage at high experimental temperatures.

where k_C, k_{tw} and k_{GND} are three coefficients, τ_{C0} is the CRSS for dislocation glide, d_{twsp} is true twin spacing, and ρ_{GND} is GND density. In Equation 13, the first term represents the yield stress of marble samples at different temperatures. This yield stress is influenced by the CRSS of the relevant slip system, the average Schmid factor of that slip system, and grain size (e.g., Harbord et al., 2023; Walker et al., 1990), which are considered to be invariant with macroscopic strain for our samples. The coefficient k_C and the CRSS thus only describe the temperature dependence of yield stress in our application (discussed in Section 4.3). In addition, dislocation density in the Taylor equation is replaced with GND density in Equation 13 to model our data. Thus, here k_{GND} of Equation 13 is not exactly equivalent to α in the Taylor equation.

The three coefficients, displayed in Figure 16a, were found by linear least-square methods applied to all the mechanical and microstructural data of this study. In this process, τ_{C0} is fixed at 196.5 MPa at room temperature, 41.0 MPa at 200°C and 16.7 MPa at 350°C by the best fit line for r slip in Figure 10 of de Bresser and Spiers (1997). State variables, $1/d_{twsp}$ and $\sqrt{\rho_{GND}}$, are from microstructural characterization of the 15 tested samples. The inversion result suggests that for unit length of state variables (i.e., twin spacing and distance between GND), the capability of increasing twin boundaries to obstruct dislocation glide is relatively greater than that of dislocation-dislocation interactions (i.e., $k_{tw} > k_{GND}$). However, given that GND significantly outnumber twins, the absolute strength is mostly contributed by the GND term (Figure 16b).

In terms of hardening, the twins and GND play roughly equal roles, with both contributing about 100 MPa of hardening over the 8% strain. More specifically, at room temperature, the amount of hardening increases linearly with strain for each of the two terms. At high experimental temperatures, most of the strain hardening is attributable to the twin-boundary term at small strain, while the GND term only has weak dependence on strain (slopes indicated in Figure 16b). In contrast, the GND term contributes to most of the hardening at intermediate strain at high experimental temperatures, while the twin-boundary term increases at a slower rate.

In the model for semi-brittle deformation at high pressure, the role of fractures is limited to accommodation of strain incompatibility. Whether the macroscopic stress is directly influenced by fracturing remains an open question but could be explored by another strain-series study at progressively lower pressures. The current model, based on an extended Taylor equation, serves as the baseline behavior with the assumption that only dislocations and twin boundaries have direct effects on the strength evolution of marble.

The relation between stress and twin density is quantified in the form of the twin-density piezometer, which is used to estimate paleostress from natural calcite (Lacombe et al., 1992; Rowe & Rutter, 1990). From our observation, the development of twin density with strain (Figure 9a) is generally consistent with the development

of stress (Figure 3a). Furthermore, strain tensor analyses of twins suggest that they serve as reliable strain indicators under low macroscopic strain conditions (typically < 4%), although their utility diminishes as strain increases.

Toward a microsphysical model, it is necessary to derive the process of microstructural development as a function of macroscopic strain and strain rate. With the assumption that plastic strain is completely accommodated by dislocations, the development of dislocation density could be modeled as

$$\frac{\mathrm{d}\rho_{\mathrm{d}}}{\mathrm{d}\varepsilon} = \frac{1}{b\lambda} - f\rho_{\mathrm{d}}, \tag{14}$$

where $f\rho_{\mathrm{d}}$ is a term for dislocation removal (Kocks, 1965; Kocks & Mecking, 2003; Rybacki et al., 2021). However, our microstructural observations suggest that dislocations accommodate only a fraction of the plastic strain. A microphysical model for semi-brittle deformation would further require consideration of comprehensive development of twinning, dislocation activity and microfracturing (e.g., Brantut, 2025). In addition, previous experiments have systematically investigated the influence of strain-rate variations on the mechanical properties of marble during semi-brittle deformation (Covey-Crump, 1994; Rybacki et al., 2021). However, the role of strain rate in governing the development of microstructures remains poorly constrained. Addressing this knowledge gap could be achieved in future studies by employing methodologies analogous to those applied in this work but with different strain rates, thereby enabling a more comprehensive understanding of strain-rate effects across both mechanical and microstructural domains. Besides, interaction between any of the two mechanisms cannot be clearly captured by the conventional EBSD mapping in this study. Further microstructural characterization by high-angular resolution EBSD and transmission electron microscopy may better resolve this issue. Alternatively, recent progress in correlating acoustic emission waveform patterns with microstructural processes may provide a new possibility for resolving more in situ microstructural information (O'Ghaffari et al., 2023). From this study, the quantitative constraints on the key microstructures provide a starting point for further microstructural investigations and microphysical modeling.

5. Conclusions

Three sets of marble samples were shortened to varying strains up to about 8% at experimental conditions that induce semi-brittle deformation. Twins, lattice curvature and intragranular microfractures were quantitatively examined by forescattered electron imaging and electron backscatter diffraction in the scanning electron microscope. The results reveal that, at small strain (strain ≤ 2%), deformation is primarily accommodated by twins. Lattice distortion, linked to GND, starts to become pronounced in the intermediate stage (strain > 2%). Intragranular fracture intensity exhibits an almost linear correlation with strain within the range of small strain and tends to stabilize at intermediate strain. Despite some nuanced variations, the overarching development of each microstructural element is similar across the different temperatures.

We found that the stress at the onset of inelasticity at room temperature is significantly greater than those at 200°C and 350°C. Such temperature dependence of the macroscopic stress is consistent with the temperature dependence of the critical resolved shear stress for *r* slip in calcite. Regarding strain hardening, we found that hindering of dislocation glide by decreasing twin spacing and increasing dislocation density is the dominant mechanism. Based on this interpretation, a phenomenological model with state variables representing the microstructural elements that hinder dislocation glide has been proposed as the extended Taylor relation. This model contains one coefficient modifying the critical resolved shear stress of *r* slip that determines the stress at the onset of inelasticity, and two coefficients that relate hardening to state variables of true twin spacing and dislocation spacing based on GND density. The microstructural data in this study provide a general overview of microstructural evolution in marble with strain and experimental conditions as a precursory basis for a microphysical model of semi-brittle deformation.

Data Availability Statement

The mechanical data and microstructural data (EBSD maps, node positions of traced fractures and twin information) have been uploaded to Zenodo at https://doi.org/10.5281/zenodo.14187374 (Qu, 2024).

Acknowledgments
Emmanuel David contributed to early technical developments on the Murrell apparatus. Technical support from Harison Wiesman, John Bowles and Neil Hughes is greatly appreciated. We thank Thomas Breithaupt, Hans de Bresser, Georg Dresen and Erik Rybacki for useful discussions. This project has received funding to N.B. from the European Research Council (ERC) under the European Union's Horizon research and innovation programme (2020 project 804685/ "RockDEaF" and 2024 project 101088963/"RockDeath"), the UK Natural Environment Research Council (Grant Agreement NE/M016471/1), and the Leverhulme Trust (Philip Leverhulme Prize). DW acknowledges support from a UK Research and Innovation Future Leaders Fellowship (Grant Agreement MR/V021788/1).

References

Alkan, S., Ojha, A., & Sehitoglu, H. (2018). Determination of latent hardening response for fenicocrmn for twin-twin interactions. *Acta Materialia*, *147*, 149–164. https://doi.org/10.1016/j.actamat.2017.12.058

Al-Shayea, N., Khan, K., & Abduljauwad, S. (2000). Effects of confining pressure and temperature on mixed-mode (I–II) fracture toughness of a limestone rock. *International Journal of Rock Mechanics and Mining Sciences*, *37*(4), 629–643. https://doi.org/10.1016/s1365-1609(00)00003-4

Amrouch, K., Lacombe, O., Bellahsen, N., Daniel, J.-M., & Callot, J.-P. (2010). Stress and strain patterns, kinematics and deformation mechanisms in a basement-cored anticline: Sheep Mountain Anticline, Wyoming. *Tectonics*, *29*(1). https://doi.org/10.1029/2009tc002525

Anderson, P. M., & Rice, J. (1986). Dislocation emission from cracks in crystals or along crystal interfaces. *Scripta Metallurgica*, *20*(11), 1467–1472. https://doi.org/10.1016/0036-9748(86)90377-7

Ashby, M. F. (1970). The deformation of plastically non-homogeneous materials. *The Philosophical Magazine: A Journal of Theoretical Experimental and Applied Physics*, *21*(170), 399–424. https://doi.org/10.1080/14786437008238426

Bak, J., Sørensen, K., Grocott, J., Korstgård, J. A., Nash, D., & Watterson, J. (1975). Tectonic implications of Precambrian shear belts in western Greenland. *Nature*, *254*(5501), 566–569. https://doi.org/10.1038/254566a0

Bernabé, Y., & Peč, M. (2024). Brittle damage processes around equi-dimensional pores or cavities in rocks: Implications for the brittle-ductile transition. *Journal of Geophysical Research: Solid Earth*, *129*(6), e2024JB028814. https://doi.org/10.1029/2024jb028814

Birch, F., & Bancroft, D. (1938). The effect of pressure on the rigidity of rocks. i. *The Journal of Geology*, *46*(1), 59–87. https://doi.org/10.1086/624620

Bönisch, M., Wu, Y., & Sehitoglu, H. (2018). Hardening by slip-twin and twin-twin interactions in FeMnNiCoCr. *Acta Materialia*, *153*, 391–403. https://doi.org/10.1016/j.actamat.2018.04.054

Bouaziz, O., & Guelton, N. (2001). Modelling of twip effect on work-hardening. *Materials Science and Engineering: A*, *319*, 246–249. https://doi.org/10.1016/s0921-5093(00)02019-0

Brace, W. F., & Kohlstedt, D. L. (1980). Limits on lithospheric stress imposed by laboratory experiments. *Journal of Geophysical Research*, *85*(B11), 6248–6252. https://doi.org/10.1029/jb085ib11p06248

Brantut, N. (2025). Semi-brittle flow of rocks: Cracks, dislocations and strain hardening. In *Proceedings A*, (Vol. 481(2307), p. 20240189). The Royal Society. https://doi.org/10.1098/rspa.2024.0189

Breithaupt, T., Katz, R. F., Hansen, L. N., & Kumamoto, K. M. (2023). Dislocation theory of steady and transient creep of crystalline solids: Predictions for olivine. *Proceedings of the National Academy of Sciences*, *120*(8), e2203448120. https://doi.org/10.1073/pnas.2203448120

Burkhard, M. (1993). Calcite twins, their geometry, appearance and significance as stress-strain markers and indicators of tectonic regime: A review. *Journal of Structural Geology*, *15*(3–5), 351–368. https://doi.org/10.1016/0191-8141(93)90132-t

Caillard, D., & Martin, J. (2003). *Thermally activated mechanisms in crystal plasticity* (Vol. 8).

Carpenter, B., Collettini, C., Viti, C., & Cavallo, A. (2016). The influence of normal stress and sliding velocity on the frictional behaviour of calcite at room temperature: Insights from laboratory experiments and microstructural observations. *Geophysical Journal International*, *205*(1), 548–561. https://doi.org/10.1093/gji/ggw038

Carter, N. L., & Kirby, S. H. (1978). *Transient creep and semibrittle behavior of crystalline rocks*. Springer.

Chandler, M. R., Meredith, P. G., Brantut, N., & Crawford, B. R. (2017). Effect of temperature on the fracture toughness of anisotropic shale and other rocks. *Geological Society, London, Special Publications*, *454*(1), 295–303. https://doi.org/10.1144/sp454.6

Chapple, W. M., & Forsyth, D. W. (1979). Earthquakes and bending of plates at trenches. *Journal of Geophysical Research*, *84*(B12), 6729–6749. https://doi.org/10.1029/jb084ib12p06729

Covey-Crump, S. (1994). The application of hart's state variable description of inelastic deformation to Carrara marble at T < 450°C. *Journal of Geophysical Research*, *99*(B10), 19793–19808. https://doi.org/10.1029/94jb01797

Dandekar, D. P. (1968). Pressure dependence of the elastic constants of calcite. *Physical Review*, *172*(3), 873–877. https://doi.org/10.1103/physrev.172.873

David, E. C., Brantut, N., & Hirth, G. (2020). Sliding crack model for nonlinearity and hysteresis in the triaxial stress-strain curve of rock, and application to antigorite deformation. *Journal of Geophysical Research: Solid Earth*, *125*(10), e2019JB018970. https://doi.org/10.1029/2019jb018970

de Bresser, J., & Spiers, C. (1990). High-temperature deformation of calcite single crystals by r+ and f+ slip. *Geological Society, London, Special Publications*, *54*(1), 285–298. https://doi.org/10.1144/gsl.sp.1990.054.01.25

de Bresser, J. (1991). *Intracrystalline deformation of calcite*. PhD thesis. Instituut voor Aardwetenschappen der Rijksuniversiteit Utrecht.

de Bresser, J. (1996). Steady state dislocation densities in experimentally deformed calcite materials: Single crystals versus polycrystals. *Journal of Geophysical Research*, *101*(B10), 22189–22201. https://doi.org/10.1029/96jb01759

de Bresser, J. (2002). On the mechanism of dislocation creep of calcite at high temperature: Inferences from experimentally measured pressure sensitivity and strain rate sensitivity of flow stress. *Journal of Geophysical Research*, *107*(B12), ECV–4. https://doi.org/10.1029/2002jb001812

de Bresser, J., & Spiers, C. (1997). Strength characteristics of the r, f, and c slip systems in calcite. *Tectonophysics*, *272*(1), 1–23. https://doi.org/10.1016/s0040-1951(96)00273-9

de Bresser, J., Urai, J., & Olgaard, D. (2005). Effect of water on the strength and microstructure of Carrara marble axially compressed at high temperature. *Journal of Structural Geology*, *27*(2), 265–281. https://doi.org/10.1016/j.jsg.2004.10.002

Edmond, J., & Paterson, M. (1972). Volume changes during the deformation of rocks at high pressures. In *International Journal of Rock Mechanics and Mining Sciences & Geomechanics Abstracts*, (Vol. 9(2), pp. 161–182). https://doi.org/10.1016/0148-9062(72)90019-8. Elsevier.

Edmond, O., & Murrell, S. (1973). Experimental observations on rock fracture at pressures up to 7 kbar and the implications for earthquake faulting. *Tectonophysics*, *16*(1–2), 71–87. https://doi.org/10.1016/0040-1951(73)90132-7

Fagereng, A., & Sibson, R. H. (2010). Mélange rheology and seismic style. *Geology*, *38*(8), 751–754. https://doi.org/10.1130/g30868.1

Fredrich, J. T., Evans, B., & Wong, T.-F. (1989). Micromechanics of the brittle to plastic transition in Carrara marble. *Journal of Geophysical Research*, *94*(B4), 4129–4145. https://doi.org/10.1029/jb094ib04p04129

Frost, H., & Ashby, M. (1982). *Deformation-mechanism maps, the plasticity and creep of metals and ceramics*. Cambridge University.

Goetze, C., & Kohlstedt, D. (1977). The dislocation structure of experimentally deformed marble. *Contributions to Mineralogy and Petrology*, *59*(3), 293–306. https://doi.org/10.1007/bf00374558

Groshong, R. H. (1972). Strain clculated from twinning in calcite. *GSA Bulletin*, *83*(7), 2025–2038. https://doi.org/10.1130/0016-7606(1972)83[2025:scftic]2.0.co;2

Guthrie, R., Jonas, J., & Asm, M. H. V. (1990). *1: Properties and selection: Irons steels and high performance alloys* (Vol. 2, p. 329). ASM international.

Hansen, L. N., Kumamoto, K. M., Thom, C. A., Wallis, D., Durham, W. B., Goldsby, D. L., et al. (2019). Low-temperature plasticity in olivine: Grain size, strain hardening, and the strength of the lithosphere. *Journal of Geophysical Research: Solid Earth*, *124*(6), 5427–5449. https://doi.org/10.1029/2018jb016736

Harbord, C., Brantut, N., David, E. C., & Mitchell, T. (2022). A high pressure, high temperature gas medium apparatus to measure acoustic velocities during deformation of rock. *Review of Scientific Instruments*, *93*(5), 053908. https://doi.org/10.1063/5.0084477

Harbord, C., Brantut, N., & Wallis, D. (2023). Grain-size effects during semi-brittle flow of calcite rocks. *Journal of Geophysical Research: Solid Earth*, *128*(8). https://doi.org/10.1029/2023jb026458

Healy, D., Rizzo, R. E., Cornwell, D. G., Farrell, N. J., Watkins, H., Timms, N. E., et al. (2017). Fracpaq: A matlab™ toolbox for the quantification of fracture patterns. *Journal of Structural Geology*, *95*, 1–16. https://doi.org/10.1016/j.jsg.2016.12.003

Heard, H., & Raleigh, C. (1972). Steady-state flow in marble at 500 to 800 C. *Geological Society of America Bulletin*, *83*(4), 935–956. https://doi.org/10.1130/0016-7606(1972)83[935:sfimat]2.0.co;2

Horii, H., & Nemat-Nasser, S. (1986). Brittle failure in compression: Splitting faulting and brittle-ductile transition. *Philosophical Transactions of the Royal Society of London - Series A: Mathematical and Physical Sciences*, *319*(1549), 337–374.

Kocks, U. (1965). A statistical theory of flow stress and work-hardening. *Philosophical Magazine*, *13*(123), 541–566. https://doi.org/10.1080/14786436608212647

Kocks, U., & Mecking, H. (2003). Physics and phenomenology of strain hardening: The fcc case. *Progress in Materials Science*, *48*(3), 171–273. https://doi.org/10.1016/s0079-6425(02)00003-8

Kohlstedt, D., & Weathers, M. S. (1980). Deformation-induced microstructures, paleopiezometers, and differential stresses in deeply eroded fault zones. *Journal of Geophysical Research*, *85*(B11), 6269–6285. https://doi.org/10.1029/jb085ib11p06269

Kohlstedt, D. L., Evans, B., & Mackwell, S. J. (1995). Strength of the lithosphere: Constraints imposed by laboratory experiments. *Journal of Geophysical Research*, *100*(B9), 17587–17602. https://doi.org/10.1029/95jb01460

Lacombe, O., Angelier, J., & Laurent, P. (1992). Determining paleostress orientations from faults and calcite twins: A case study near the sainte-victoire range (southern France). *Tectonophysics*, *201*(1–2), 141–156. https://doi.org/10.1016/0040-1951(92)90180-e

Lawn, B. (1993). *The griffith concept, chapter 1, page 1*. Cambridge University Press.

Lin, C.-C. (2013). Elasticity of calcite: Thermal evolution. *Physics and Chemistry of Minerals*, *40*(2), 157–166. https://doi.org/10.1007/s00269-012-0555-3

Liu, D., & Brantut, N. (2023). Micromechanical controls on the brittle-plastic transition in rocks. *Geophysical Journal International*, *234*(1), 562–584. https://doi.org/10.1093/gji/ggad065

Mecking, H., & Kocks, U. (1981). Kinetics of flow and strain-hardening. *Acta Metallurgica*, *29*(11), 1865–1875. https://doi.org/10.1016/0001-6160(81)90112-7

Mitchell, T., & Hirth, J. (1991). The shape, configuration and stress field of twins and martensite plates. *Acta Metallurgica et Materialia*, *39*(7), 1711–1717. https://doi.org/10.1016/0956-7151(91)90260-8

Muransky, O., Balogh, L., Tran, M., Hamelin, C., Park, J.-S., & Daymond, M. R. (2019). On the measurement of dislocations and dislocation substructures using EBSD and HRSD techniques. *Acta Materialia*, *175*, 297–313. https://doi.org/10.1016/j.actamat.2019.05.036

Murrell, S., Meredith, P., Sammonds, P., Ayling, M., & Jones, C. (1989). High temperature triaxial apparatus for acoustic measurements. In *ISRM international symposium*. ISRM.

Nes, E. (1997). Modelling of work hardening and stress saturation in FCC metals. *Progress in Materials Science*, *41*(3), 129–193. https://doi.org/10.1016/s0079-6425(97)00032-7

Nicolas, A., Fortin, J., & Guéguen, Y. (2017). Micromechanical constitutive model for low-temperature constant strain rate deformation of limestones in the brittle and semi-brittle regime. *Geophysical Journal International*, *211*(1), 300–321. https://doi.org/10.1093/gji/ggx299

Nye, J. F. (1953). Some geometrical relations in dislocated crystals. *Acta Metallurgica*, *1*(2), 153–162. https://doi.org/10.1016/0001-6160(53)90054-6

O'Ghaffari, H., Pec, M., Mittal, T., Mok, U., Chang, H., & Evans, B. (2023). Microscopic defect dynamics during a brittle-to-ductile transition. *Proceedings of the National Academy of Sciences*, *120*(42), e2305667120. https://doi.org/10.1073/pnas.2305667120

Olsson, W. A. (1974). Microfracturing and faulting in a limestone. *Tectonophysics*, *24*(3), 277–285. https://doi.org/10.1016/0040-1951(74)90012-2

Olsson, W. A., & Peng, S. S. (1976). Microcrack nucleation in marble. *International Journal of Rock Mechanics and Mining Sciences & Geomechanics Abstracts*, *13*(2), 53–59. https://doi.org/10.1016/0148-9062(76)90704-x

Passchier, C. (1982). Pseudotachylyte and the development of ultramylonite bands in the Saint-Barthélemy Massif, French pyrenees. *Journal of Structural Geology*, *4*(1), 69–79. https://doi.org/10.1016/0191-8141(82)90008-6

Pec, M., Stünitz, H., Heilbronner, R., & Drury, M. (2016). Semi-brittle flow of granitoid fault rocks in experiments. *Journal of Geophysical Research: Solid Earth*, *121*(3), 1677–1705. https://doi.org/10.1002/2015jb012513

Qu, T. (2024). Mechanical and microstructural data for strain series on marble [Dataset]. *Zenodo*. https://doi.org/10.5281/zenodo.14187375

Quintanilla-Terminel, A., & Evans, B. (2016). Heterogeneity of inelastic strain during creep of Carrara marble: Microscale strain measurement technique. *Journal of Geophysical Research: Solid Earth*, *121*(8), 5736–5760. https://doi.org/10.1002/2016jb012970

Rowe, K., & Rutter, E. (1990). Palaeostress estimation using calcite twinning: Experimental calibration and application to nature. *Journal of Structural Geology*, *12*(1), 1–17. https://doi.org/10.1016/0191-8141(90)90044-y

Rutter, E., Wallis, D., & Kosiorek, K. (2022). Application of electron backscatter diffraction to calcite-twinning paleopiezometry. *Geosciences*, *12*(6), 222. https://doi.org/10.3390/geosciences12060222

Rutter, E. H. (1983). Pressure solution in nature, theory and experiment. *Journal of the Geological Society*, *140*(5), 725–740. https://doi.org/10.1144/gsjgs.140.5.0725

Rybacki, E., Evans, B., Janssen, C., Wirth, R., & Dresen, G. (2013). Influence of stress, temperature, and strain on calcite twins constrained by deformation experiments. *Tectonophysics*, *601*, 20–36. https://doi.org/10.1016/j.tecto.2013.04.021

Rybacki, E., Janssen, C., Wirth, R., Chen, K., Wenk, H.-R., Stromeyer, D., & Dresen, G. (2011). Low-temperature deformation in calcite veins of SAFOD core samples (San Andreas Fault)—Microstructural analysis and implications for fault rheology. *Tectonophysics*, *509*(1–2), 107–119. https://doi.org/10.1016/j.tecto.2011.05.014

Rybacki, E., Niu, L., & Evans, B. (2021). Semi-brittle deformation of Carrara marble: Hardening and twinning induced plasticity. *Journal of Geophysical Research: Solid Earth*, *126*(12), e2021JB022573. https://doi.org/10.1029/2021jb022573

Sandiford, D., & Craig, T. J. (2023). Plate bending earthquakes and the strength distribution of the lithosphere. *Geophysical Journal International*, *235*(1), 488–508. https://doi.org/10.1093/gji/ggad230

Schmid, S. M., Paterson, M. S., & Boland, J. N. (1980). High temperature flow and dynamic recrystallization in carrara marble. *Tectonophysics*, *65*(3–4), 245–280. https://doi.org/10.1016/0040-1951(80)90077-3

Seybold, L., Trepmann, C. A., Hölzl, S., Pollok, K., Langenhorst, F., Dellefant, F., & Kaliwoda, M. (2023). Twinned calcite as an indicator of high differential stresses and low shock pressure conditions during impact cratering. *Meteoritics & Planetary Science*, *58*(9), 1287–1305. https://doi.org/10.1111/maps.14056

Shimamoto, T. (1986). Transition between frictional slip and ductile flow for halite shear zones at room temperature. *Science*, *231*(4739), 711–714. https://doi.org/10.1126/science.231.4739.711

Sibson, R. H. (1977). Fault rocks and fault mechanisms. *Journal of the Geological Society*, *133*(3), 191–213. https://doi.org/10.1144/gsjgs.133.3.0191

Sibson, R. H. (1982). Fault zone models, heat flow, and the depth distribution of earthquakes in the continental crust of the United States. *Bulletin of the Seismological Society of America*, *72*(1), 151–163.

Skemer, P., Katayama, I., Jiang, Z., & Karato, S.-i. (2005). The misorientation index: Development of a new method for calculating the strength of lattice-preferred orientation. *Tectonophysics*, *411*(1–4), 157–167. https://doi.org/10.1016/j.tecto.2005.08.023

Taylor, G. I. (1934). The mechanism of plastic deformation of crystals. Part I.—Theoretical. *Proceedings of the Royal Society of London - Series A: Containing Papers of a Mathematical and Physical Character*, *145*(855), 362–387.

Thom, C. A., Hansen, L. N., Breithaupt, T., Goldsby, D. L., & Kumamoto, K. M. (2022). Backstresses in geologic materials quantified by nanoindentation load-drop experiments. *Philosophical Magazine*, *102*(19), 1974–1988. https://doi.org/10.1080/14786435.2022.2100937

von Mises, R. (1928). Mechanik der plastischen formänderung von kristallen. *ZAMM-Journal of Applied Mathematics and Mechanics/Zeitschrift für Angewandte Mathematik und Mechanik*, *8*(3), 161–185. https://doi.org/10.1002/zamm.19280080302

Walker, A., Rutter, E., & Brodie, K. (1990). Experimental study of grain-size sensitive flow of synthetic, hot-pressed calcite rocks. *Geological Society*, *54*(1), 259–284. https://doi.org/10.1144/gsl.sp.1990.054.01.24

Wallis, D., Hansen, L. N., Britton, T. B., & Wilkinson, A. J. (2016). Geometrically necessary dislocation densities in olivine obtained using high-angular resolution electron backscatter diffraction. *Ultramicroscopy*, *168*, 34–45. https://doi.org/10.1016/j.ultramic.2016.06.002

Walsh, J. (1965). The effect of cracks on the uniaxial elastic compression of rocks. *Journal of Geophysical Research*, *70*(2), 399–411. https://doi.org/10.1029/jz070i002p00399

Walsh, J. (1966). Seismic wave attenuation in rock due to friction. *Journal of Geophysical Research*, *71*(10), 2591–2599. https://doi.org/10.1029/jz071i010p02591

Watt, J. P., & Peselnick, L. (1980). Clarification of the Hashin-Shtrikman bounds on the effective elastic moduli of polycrystals with hexagonal, trigonal, and tetragonal symmetries. *Journal of Applied Physics*, *51*(3), 1525–1531. https://doi.org/10.1063/1.327804

Weertman, J., & Weertman, J. (1971). *Elementary dislocation theory*. Oxford University Press.

White, J. t., & White, S. (1983). Semi-brittle deformation within the Alpine fault zone, New Zealand. *Journal of Structural Geology*, *5*(6), 579–589. https://doi.org/10.1016/0191-8141(83)90070-6

Xu, L., & Evans, B. (2010). Strain heterogeneity in deformed Carrara marble using a microscale strain mapping technique. *Journal of Geophysical Research*, *115*(B4). https://doi.org/10.1029/2009jb006458